The Astrophysical Journal, 755:60 (16pp), 2012 August 10 doi:10.1088/0004-637X/755/1/60

REVERBERATION MAPPING RESULTS FOR FIVE SEYFERT 1 GALAXIES

C. J. Grier[1], B. M. Peterson[1,2], R. W. Pogge[1,2], K. D. Denney[3], M. C. Bentz[4], Paul Martini[1,2], S. G. Sergeev[5], S. Kaspi[6,7], T. Minezaki[8], Y. Zu[1], C. S. Kochanek[1,2], R. Siverd[9], B. Shappee[1], K. Z. Stanek[1,2], C. Araya Salvo[1], T. G. Beatty[1], J. C. Bird[1], D. J. Bord[10], G. A. Borman[5,11], X. Che[12], C. Chen[13], S. A. Cohen[13], M. Dietrich[1], V. T. Doroshenko[5,11,14], T. Drake[4], Yu. S. Efimov[5,16], N. Free[15], I. Ginsburg[13], C. B. Henderson[1], A. L. King[12], S. Koshida[8], K. Mogren[1], M. Molina[1], A. M. Mosquera[1], S. V. Nazarov[5,11], D. N. Okhmat[5,11], O. Pejcha[1], S. Rafter[7], J. C. Shields[15], J. Skowron[1], D. M. Szczygiel[1], M. Valluri[12], and J. L. van Saders[1]

[1] Department of Astronomy, The Ohio State University, 140 West 18th Avenue, Columbus, OH 43210, USA
[2] Center for Cosmology & AstroParticle Physics, The Ohio State University, 191 West Woodruff Avenue, Columbus, OH 4321, USA
[3] Marie Curie Fellow at the Dark Cosmology Centre, Niels Bohr Institute, University of Copenhagen, Juliane Maries Vej 30, DK-2100 Copenhagen, Denmark
[4] Department of Physics and Astronomy, Georgia State University, Astronomy Offices, One Park Place South SE, Suite 700, Atlanta, GA 30303, USA
[5] Crimean Astrophysical Observatory, P/O Nauchny Crimea 98409, Ukraine
[6] School of Physics and Astronomy, Raymond and Beverly Sackler Faculty of Exact Sciences, Tel Aviv University, Tel Aviv 69978, Israel
[7] Physics Department, Technion, Haifa 32000, Israel
[8] Institute of Astronomy, School of Science, University of Tokyo, 2-21-1, Osawa, Mitaka, 181-0015, Tokyo, Japan
[9] Department of Physics and Astronomy, Vanderbilt University, 5301 Stevenson Center, Nashville, TN 37235, USA
[10] Department of Natural Sciences, The University of Michigan-Dearborn, 4901 Evergreen Road, Dearborn, MI 48128, USA
[11] Isaac Newton Institute of Chile, Crimean Branch, Ukraine
[12] Department of Astronomy, University of Michigan, 500 Church Street, Ann Arbor, MI 41809, USA
[13] Department of Physics and Astronomy, Dartmouth College, 6127 Wilder Laboratory, Hanover, NH 03755, USA
[14] South Station of the Moscow MV Lomonosov State University, Moscow, Russia, P/O Nauchny, 98409 Crimea, Ukraine
[15] Department of Physics & Astronomy, Ohio University, Athens, OH 45701, USA
Received 2012 April 4; accepted 2012 June 22; published 2012 July 26

ABSTRACT

We present the results from a detailed analysis of photometric and spectrophotometric data on five Seyfert 1 galaxies observed as a part of a recent reverberation mapping program. The data were collected at several observatories over a 140 day span beginning in 2010 August and ending in 2011 January. We obtained high sampling-rate light curves for Mrk 335, Mrk 1501, 3C 120, Mrk 6, and PG 2130+099, from which we have measured the time lag between variations in the 5100 Å continuum and the Hβ broad emission line. We then used these measurements to calculate the mass of the supermassive black hole at the center of each of these galaxies. Our new measurements substantially improve previous measurements of $M_{\rm BH}$ and the size of the broad line-emitting region for four sources and add a measurement for one new object. Our new measurements are consistent with photoionization physics regulating the location of the broad line region in active galactic nuclei.

Key words: galaxies: active – galaxies: nuclei – galaxies: Seyfert

Online-only material: color figures

1. INTRODUCTION

In the past two decades, several correlations have been observed between various properties of galaxies and the masses of their central supermassive black holes (BHs). Two of the best-studied correlations, in both active and quiescent galaxies, are the relations between the mass of the central black hole ($M_{\rm BH}$) and the stellar velocity dispersion of the host bulge, commonly known as the $M_{\rm BH}$–σ_* relation (e.g., Ferrarese & Merritt 2000; Gebhardt et al. 2000, Tremaine et al. 2002; Onken et al. 2004; Woo et al. 2010), and the relation between $M_{\rm BH}$ and the luminosity of the host bulge, also referred to as the $M_{\rm BH}$–$L_{\rm Bulge}$ relation (e.g., Kormendy & Richstone 1995; Magorrian et al. 1998; Bentz et al. 2009b; Gültekin et al. 2009). The existence of these correlations suggests that there is a connection between supermassive BH growth and galaxy evolution. If this connection exists, simulations or theories of galaxy and BH growth must naturally produce these observed correlations. Explanations for the observed $M_{\rm BH}$–galaxy correlations have ranged from hierarchical mergers and quasar feedback to self-regulated BH growth (e.g., Silk & Rees 1998; Di Matteo et al. 2005; Hopkins et al. 2009), although there are also arguments that it is simply a consequence of random mergers (e.g., Peng 2007; Peng 2010; Jahnke & Macciò 2011).

A large sample of accurate direct $M_{\rm BH}$ measurements is crucial to understanding this BH–galaxy connection. Because the BH sphere of influence is much too small to be resolvable in any but the nearest galaxies, the only direct method of measuring $M_{\rm BH}$ in distant galaxies is reverberation mapping (Blandford & McKee 1982; Peterson 1993), which is applicable to Type 1, or broad-line, active galactic nuclei (AGNs). Reverberation mapping relies on the correlation between variations of the AGN continuum emission and the subsequent response of the broad emission lines. By monitoring AGN spectra over a period of time, one can measure the radius of the broad line region by observing the time delay, or "lag," between fluctuations in the continuum and emission-line fluxes, which is due to light travel time between the continuum source and the BLR. Assuming the gas is in virial motion, this BLR radius, $R_{\rm BLR}$, can be combined with some measure of the BLR gas velocity from the Doppler-broadened emission-line widths to obtain an estimate of $M_{\rm BH}$. To date, this method has been applied to measure BLR radii and

[16] Deceased, 2011 October 21.

Table 1
Object List

Object	R.A. (J2000)	Decl. (J2000)	z	A_B[a] (mag)
Mrk 335	00 06 19.5	+20 12 10	0.0258	0.153
Mrk 1501	00 10 31.0	+10 58 30	0.0893	0.422
3C 120	04 33 11.1	+05 21 16	0.0330	1.283
Mrk 6	06 52 12.2	+74 25 37	0.0188	0.585
PG 2130+099	21 32 27.8	+10 08 19	0.0630	0.192

Note. [a] Galactic extinctions are from Schlegel et al. (1998).

Table 2
Spectroscopic and Photometric Observations

	Spectroscopy			Photometry		
Object	Observatory	N_{obs}	HJD (−2450000)	Observatory	N_{obs}	HJD (−2450000)
Mrk 335	MDM	78	5440–5559	CrAO	25	5431–5569
	CrAO	7	5509–5568	WISE	19	5511–5545
Mrk 1501	MDM	62	5440–5559	CrAO	63	5430–5568
	CrAO	18	5443–5568	WISE	64	5433–5541
3C 120	MDM	69	5441–5559	CrAO	64	5430–5568
	CrAO	15	5456–5569	WISE	43	5436–5545
Mrk 6	MDM	75	5441–5562	CrAO	59	5430–5569
	CrAO	21	5443–5539	WISE	50	5435–5545
PG 2130+099	MDM	68	5441–5557	CrAO	74	5430–5556
	CrAO	20	5443–5539	WISE	72	5433–5541

M_{BH} in nearly 50 AGNs (e.g., Peterson et al. 2004; Bentz et al. 2009c; Denney et al. 2010). See Marziani & Sulentic (2012) for a recent review on using the BLR to measure M_{BH}.

These measurements have confirmed the existence of a correlation predicted by photoionization theory between the radius of the BLR and the AGN continuum luminosity, known as the R_{BLR}–L relation (e.g., Davidson 1972; Davidson & Netzer 1979). This correlation allows one to obtain both velocity and R_{BLR} estimates from a single calibrated spectrum, and has been used to calculate M_{BH} in large samples of AGNs (e.g., Shen et al. 2008). This can be used to investigate the evolution of the BH mass function (e.g., Greene & Ho 2007; Vestergaard et al. 2008; Vestergaard & Osmer 2009; Kelly et al. 2010), the growth of BHs compared to their hosts, the Eddington ratios of quasars (e.g., Kollmeier et al. 2006; Kelly et al. 2010), and even the dependence of accretion disk sizes on BH mass (Morgan et al. 2010). The existence of local correlations between host properties and M_{BH} provides another means of exploring BH populations, where BH masses can be inferred from the properties of their hosts. However, there has recently been some discussion on the nature of these correlations, especially the M_{BH}–σ_* relation. In these applications, the M_{BH}–σ_* relation is assumed to be similar in quiescent and active galaxies, but there are claims that many AGNs lie below or above the M_{BH}–σ_* relation at both the high- and low-luminosity ends (see, for example, Dasyra et al. 2007; Greene et al. 2010; Mathur et al. 2011). Whether or not M_{BH} estimates based on these relationships are reliable is openly debated. Continuing to make new and improved M_{BH} measurements using reverberation mapping is one way to investigate this.

Light curve quality, in terms of sampling density, duration, and precision flux measurements, is a very important factor in reverberation measurements. In particular, light curves that are too short in duration or inadequately sampled can result in incorrect lag measurements (e.g., Perez et al. 1992; Welsh 1999; Grier et al. 2008). Since the 1990s, our view of what constitutes "adequately sampled" has changed dramatically, and we now know that some of the early measurements need to be redone, as their sampling rates are low enough that we have serious doubts about their suitability in recovering BLR radii. In a continuing effort to improve the database of reverberation-mapped objects, we carried out a massive reverberation mapping program at multiple institutions beginning in 2010 August and running until 2011 January. The main goals of our program were (1) to re-observe old objects lacking well-sampled light curves, (2) to expand the reverberation-mapped sample by observing new objects, (3) to obtain velocity-delay maps for several of the targets, and (4) if possible, to measure a reverberation lag in the high-ionization He II λ4686 emission line in a narrow-line Seyfert 1 galaxy (Mrk 335 in this case, with results published in Grier et al. 2012). We limited our target list to galaxies with expected time lags that were short enough to allow successful measurements during our four-month long campaign. Our final target list included eight objects, and we succeeded in measuring lags for six. Two objects, NGC 4151 and NGC 7603, were dropped due to weather-related time losses. Here we present lag measurements for five of the six remaining objects, while the sixth object, NGC 7469, presents us with a number of interesting challenges and will be discussed in a future work. These five targets and their basic properties are listed in Table 1. We will discuss velocity-delay maps in a forthcoming study.

2. OBSERVATIONS

In general, we follow the observational and data reduction practices of Denney et al. (2010) for the spectroscopic observations. Our data analysis methods follow those of Peterson et al. (2004). A brief summary and any deviations from these methodologies are discussed below. When needed, we adopt a cosmological model with $\Omega_m = 0.3$, $\Omega_\Lambda = 0.70$, and $H_0 = 70$ km s^{-1} Mpc^{-1}.

2.1. Spectroscopy

The majority of the spectra were obtained using the MDM Observatory 1.3 m McGraw-Hill telescope on Kitt Peak. We used the Boller and Chivens CCD spectrograph to obtain spectra over the course of 120 nights from 2010 August 31 to December 28. We used the 350 mm^{-1} grating to obtain a dispersion of 1.33 Å pixel^{-1}. We set the grating for a central wavelength of 5150 Å, which resulted in spectral coverage from roughly 4400 Å to 5850 Å. The slit was oriented north–south (position angle = 0) and set to a width of 5.″0, which resulted in a spectral resolution of 7.9 Å. We used an extraction window of 12.″75 along the slit. We also obtained spectra during this time period using the 2.6 m Shajn telescope at the Crimean Astrophysical Observatory (CrAO). These data were acquired with the Nasmith spectrograph and SPEC-10 CCD. A 3.″0 slit was used at a position angle of 90°, and we used an extraction window of 13.″0. Because of the large slit size used, there should be no effect on the AGN light due to the change in the position angle between the MDM and CrAO spectra. However, this will affect the amount of host galaxy light received through the slit. The spectral coverage in the CrAO data was from approximately 3900 Å to 6100 Å, with a dispersion of 1.0 Å pixel^{-1}. Table 2 lists the number of spectroscopic observations and time coverage at each telescope for our sample.

The reduced spectra were calibrated onto an absolute flux scale by assuming that the [O III] λ5007 narrow-line flux is

Table 3
Spectral Properties

Objects (1)	FWHM([O III] λ5007)[a] Rest Frame (km s^{-1}) (2)	F([O III]λ5007) (10^{-13} erg s^{-1} cm^{-2}) (3)	$F_{\rm Host}$(5100 Å) (10^{-15} erg s^{-1} cm^{-2} Å^{-1}) (4)
Mrk 335	280	2.31 ± 0.10[b]	1.70 ± 0.16
Mrk 1501	...	1.13 ± 0.02[c]	...
3C 120	...	3.67 ± 0.07[c]	0.685 ± 0.063
Mrk 6	475	7.17 ± 0.12[c]	...
PG 2130+099	350	1.36 ± 0.10[d]	0.601 ± 0.055

Notes.
[a] From Whittle (1992).
[b] From Peterson et al. (1998).
[c] This work.
[d] From Grier et al. (2008).

constant. The reference spectra for this calibration were created by averaging spectra taken on photometric nights for each source. We scaled these reference spectra to the absolute flux of the [O III] λ5007 line for each object (listed in Column 3 of Table 3) to create an absolute flux-calibrated reference spectrum for each object. We confirmed that the [O III] λ5007 fluxes in these reference spectra agreed with previous measurements, where available. Our new measurement of F([O III] λ5007) = 3.67×10^{-13} erg s^{-1} cm^{-2} for 3C 120 was larger than that of Peterson et al. (1998), who measured F([O III] λ5007) = 3.02×10^{-13} erg s^{-1} cm^{-2}. Since our spectra have improved greatly in quality since then we adopt our new [O III] λ5007 flux. We did not find a published absolute [O III] λ5007 flux measurement for Mrk 1501, so for that source we adopt the flux measured in our average spectrum of the photometric data as the absolute [O III] flux. Using a χ^2 goodness-of-fit estimator method to minimize the flux differences between the spectra (van Groningen & Wanders 1992), we then scaled each individual spectrum to the reference spectrum. These procedures yield an absolute flux-calibrated data set for each object from which to measure the mean AGN luminosity. In some spectra, we were unable to obtain a good fit due to changes in spectrograph focus, so we manually scaled these spectra instead. Figure 1 shows the calibrated mean and root-mean-square residual (rms) spectra of our five objects based on the calibrated MDM spectra.

2.2. Photometry

To supplement our spectra, we obtained V-band imaging observations using the 70 cm telescope at CrAO and the 46 cm Centurion telescope at Wise Observatory of Tel Aviv University. The CrAO observations used the AP7p CCD, which has 512 × 512 pixels with a 15′ × 15′ field of view when mounted at prime focus. The Wise Observatory used an STL-6303E CCD with 3072 × 2048 pixels, with a field of view of 75′ × 50′ for our setup. A summary of the photometric observations can be found in Table 2, including the number of observations of each object at each telescope and their span in heliocentric Julian date (HJD).

3. LIGHT CURVES

3.1. Spectroscopic Light Curves

Emission-line light curves were created for both the MDM and CrAO data sets by fitting a linear continuum underneath the Hβ line in each spectrum and integrating the flux above it. The continuum was defined by two regions adjacent to the emission line, which is defined by regions given in Table 4.

Table 4
Continuum and Emission-line Integration Regions

Object	Continuum Integration Region[a] (Å)	Hβ Integration Region[a] (Å)
Mrk 335	5215–5240	4910–5100
Mrk 1501	5540–5560	5190–5540
3C 120	5250–5295	4930–5140
Mrk 6	5140–5175	4820–5140
PG 2130+099	5420–5435	5085–5284

Note. [a] All integration regions are in the observed frame.

For the MDM data, the 5100 Å continuum light curves were created by taking the average flux measured in the wavelength regions listed in Table 4. Initial CrAO continuum and Hβ light curves were created the same way—however, the CrAO spectra were on a different flux scale than the MDM spectra because different amounts of [O III] and host galaxy light enter their slits due to changes in seeing, slit orientation, and aperture size. We assumed that there is no real variability on timescales of less than 0.5 days, so we calibrated the CrAO light curves to the MDM light curves by multiplying the fluxes by a constant calculated by taking the average flux ratios between pairs of observations from the CrAO and MDM light curves that are separated by less than 0.5 days, putting both light curves on the same flux scale.

3.2. Photometric Light Curves

For the WISE imaging data, we used image subtraction to produce the light curves using ISIS (Alard & Lupton 1998; Alard 2000). We generally follow the procedures of Shappee & Stanek (2011). The images are first aligned using a program called Sexterp (R. Siverd 2012, in preparation). Sexterp is a replacement for ISIS' default interp.csh that relies on SExtractor (Bertin & Arnouts 1996) for source identification. SExtractor source lists are significantly more robust and improve registration accuracy. We additionally use an upgraded interpolation utility provided with Sexterp. This routine implements the publicly available Bspline interpolation code of Thévenaz et al. (2000) and produced better results with our images.

We then used ISIS to create a reference image for each field using the 20–30 images with the best seeing and lowest background counts. When creating the reference image, ISIS convolves the images with a spatially variable convolution kernel to transform all images to the same point-spread function (PSF) and background level. The resulting images are then stacked using a 3σ rejection limit from the median. We then used ISIS to convolve the reference image with a kernel to match it to

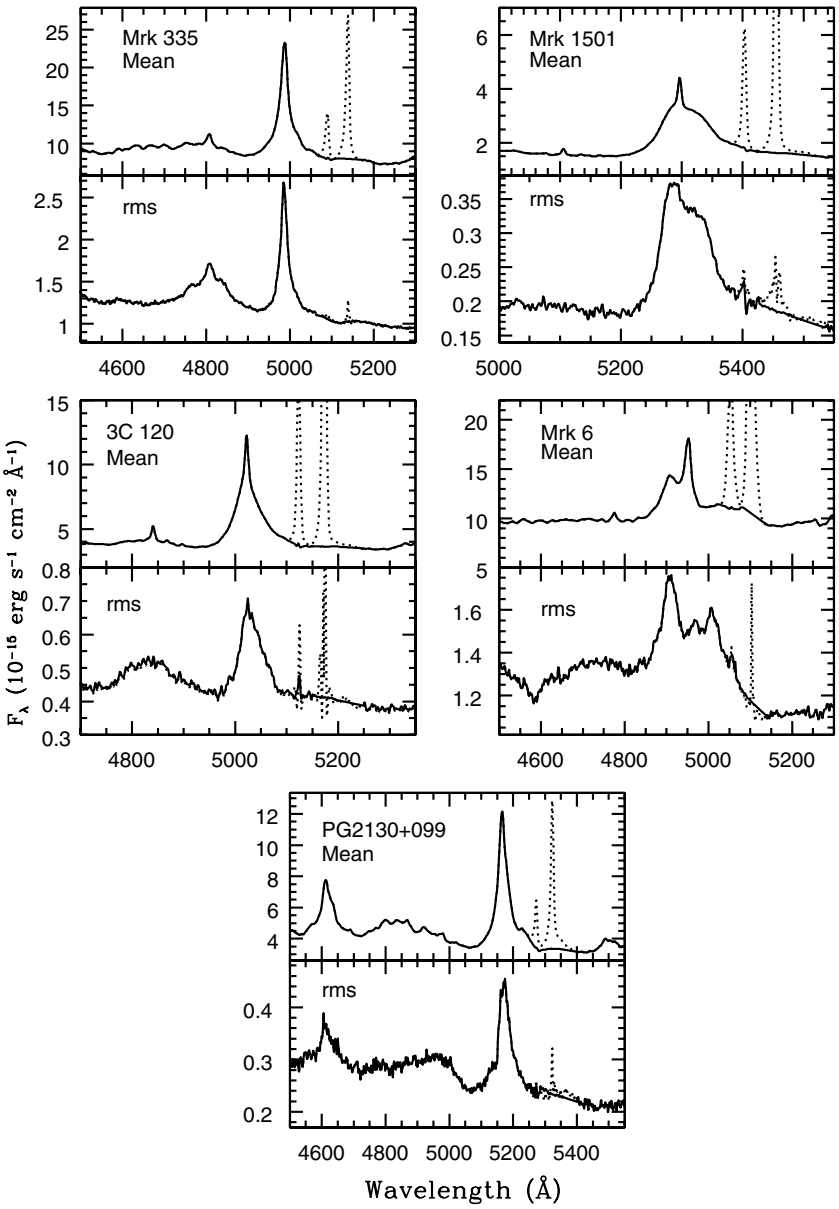

Figure 1. Flux-calibrated mean and rms residual spectra of each object. All spectra are shown in the observed frame with the flux density in units of 10^{-15} erg s^{-1} cm^{-2} Å^{-1}. The dotted lines show that the spectra before the [O III] narrow emission lines have been subtracted, while the solid line shows the spectra after the subtraction. Note that we did not remove a narrow component of the Hβ emission line.

each individual image in the data set and subtract each individual frame from its corresponding convolved reference image. We then extract light curves for the nucleus of each galaxy using ISIS to place a PSF-weighted aperture over the nucleus and measure the residual flux. We used varying extraction apertures for the different objects, choosing apertures large enough to account for all AGN light but minimizing the host galaxy light included. For the CrAO images, we used photometric fluxes based on standard aperture photometry, which were measured within an aperture of 15.″0. This includes all of the host galaxy flux for most of our objects and was chosen to minimize slit losses due to variable seeing. See Sergeev et al. (2005) for more details on obtaining the CrAO photometric fluxes.

3.3. Combined Light Curves

The spectroscopic continuum light curves were merged with the photometric light curves as follows. We applied a multiplicative scale factor as well as an additive flux adjustment to each photometric light curve to put them all on the same scale and correct for the differences in host galaxy starlight that enters the apertures (see Peterson et al. 1995). The final continuum and emission-line light curves, scaled to our MDM light curves, are shown in Figure 2. The continuum and Hβ fluxes are given in Tables 5 and 6 and labeled according to the observatory at which they were obtained. Final light curve statistics are given in Table 7.

4. TIME-SERIES MEASUREMENTS

Previous reverberation studies have relied on fairly simple cross-correlation methods to measure the time delay between the continuum and emission-line variations, τ. Recently, however, Zu et al. (2011) introduced an alternative method of measuring reverberation time lags called stochastic process estimation for

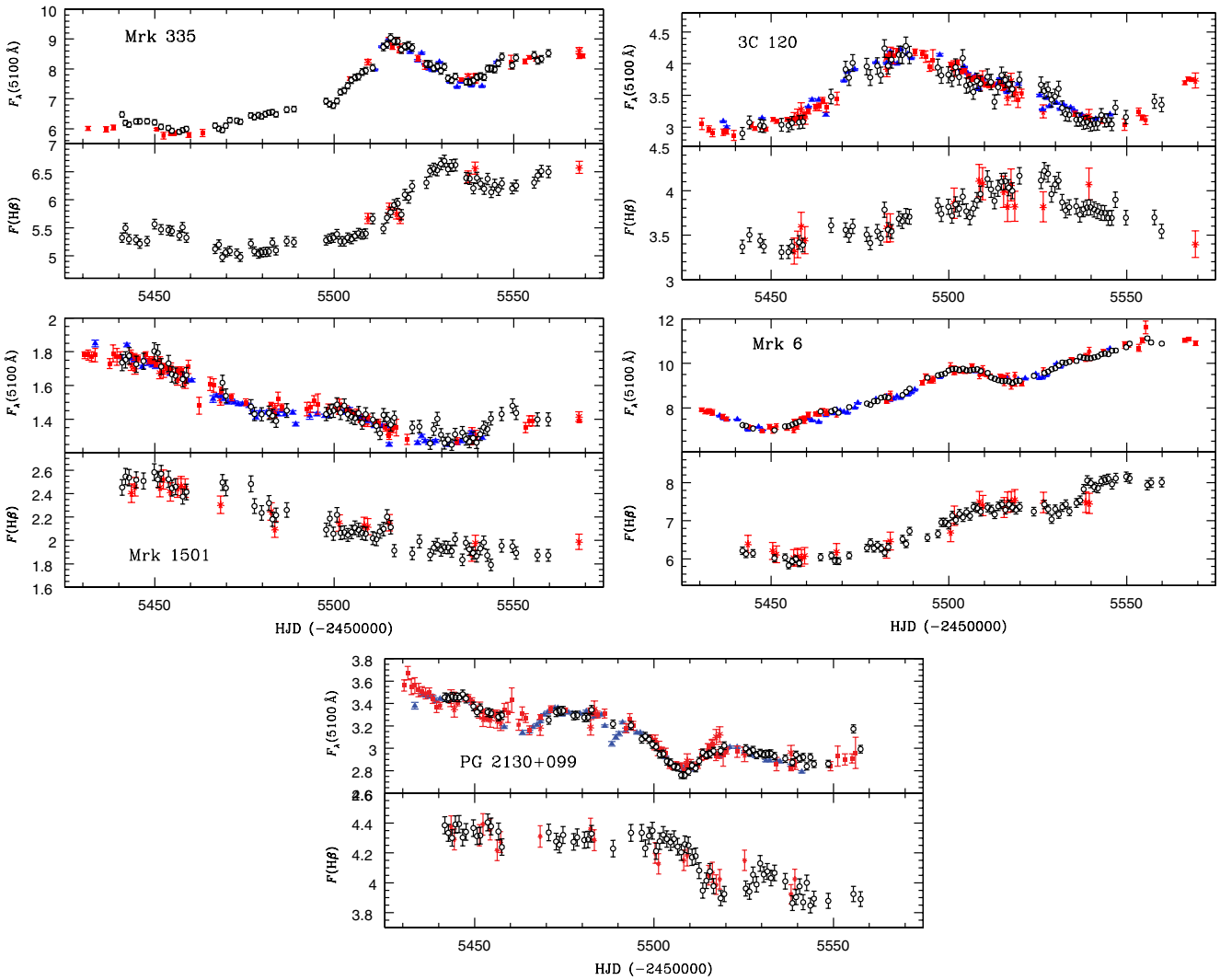

Figure 2. Complete light curves for the five objects observed during our campaign. For each object, the top panel shows the 5100 Å flux in units of 10^{-15} erg s^{-1} cm^{-2} Å^{-1} and the bottom panel shows the integrated H$\beta\lambda$4861 flux in units of 10^{-13} erg s^{-1} cm^{-2}. Open black circles denote the observations from MDM Observatory and red asterisks represent spectra taken at CrAO. Closed red squares show the photometric observations from CrAO, and closed blue triangles represent photometric observations from the WISE Observatory.

(A color version of this figure is available in the online journal.)

AGN reverberation (SPEAR[17]), and demonstrated its ability to recover accurate time lags. We utilize this method here. As with cross-correlation, we assume all emission-line light curves are scaled and shifted versions of the continuum light curve. SPEAR differs from simple cross-correlation methods in two basic respects. First, SPEAR explicitly builds a model of the light curve and transfer function and fits it to both the continuum and the line data, maximizing the likelihood $\mathscr{L}$ of the model and then computing uncertainties using the (Bayesian) Markov chain Monte Carlo method. Second, as part of this process it models the continuum light curve as an autoregressive process using a damped random walk (DRW) model. It has long been known that AGN continuum variability can be modeled as an autoregressive process (Gaskell & Peterson 1987) and a DRW model has been demonstrated to be a good statistical model of quasar variability using large ($\sim 10^4$) samples of quasar light curves (e.g., Kelly et al. 2009; Kozłowski et al. 2010; MacLeod et al. 2010; Zu et al. 2012). The parameters of the DRW model are included in the fits and their uncertainties, as is a simple top-hat model of the transfer function and the light curve means (or trends if desired).

The key physical advantage of SPEAR is that it automatically includes a self-consistent, physical model of how to interpolate in time. For any given DRW model parameters, the stochastic process model gives a mathematical estimate for the light curve at any time along with its uncertainties that naturally includes all the information in both the continuum and line light curves and their uncertainties. Since the DRW parameters also have to be estimated from the data, we allow them to vary as part of the overall model as well. In essence, this leads to a lag estimate that naturally includes the uncertainties in how to interpolate between data points, constrained by the physical properties of the variability in the target. Because it is then a statistical fit to the data with a set of parameters and a standard likelihood function, it also allows the use of powerful statistical methods like Markov chain Monte Carlo methods to produce uncertainties that correctly incorporate the effects of the model uncertainties on the lag estimate.

We used SPEAR on our light curves using the code described by Zu et al. (2011) and successfully measured time lags ($\tau_{\rm SPEAR}$)

[17] Available at http://www.astronomy.ohio-state.edu/~yingzu/spear.html

Table 5
V Band and Continuum Fluxes

Mrk 335		Mrk 1501		3C 120		Mrk 6		PG 2130+099	
HJD[a]	F_{con}[b]	HJD[a]	F_{con}[b]	HJD[a]	F_{con}[b]	HJD[a]	F_{con}[b]	HJD[a]	F_{con}[b]
5431.450 A	6.010 ± 0.070	5430.48 A	1.780 ± 0.020	5430.580 A	3.050 ± 0.090	5430.548 A	7.930 ± 0.070	5430.38 A	3.560 ± 0.050
5436.450 A	5.980 ± 0.090	5431.48 A	1.780 ± 0.030	5432.570 A	2.970 ± 0.050	5431.526 A	7.830 ± 0.090	5431.38 A	3.670 ± 0.060
5438.460 A	6.040 ± 0.080	5432.48 A	1.770 ± 0.030	5433.550 A	2.910 ± 0.060	5432.517 A	7.850 ± 0.110	5432.38 A	3.550 ± 0.070
5440.908 M	6.478 ± 0.091	5433.41 W	1.850 ± 0.020	5436.560 A	2.920 ± 0.050	5433.491 A	7.800 ± 0.130	5433.32 A	3.560 ± 0.070
5441.869 M	6.196 ± 0.087	5433.43 A	1.780 ± 0.040	5436.600 W	3.090 ± 0.010	5435.574 W	7.650 ± 0.020	5433.36 W	3.380 ± 0.030
5442.838 M	6.142 ± 0.087	5437.47 A	1.730 ± 0.030	5437.550 A	2.930 ± 0.040	5436.482 A	7.610 ± 0.100	5434.37 A	3.520 ± 0.060
5444.840 M	6.244 ± 0.088	5438.42 A	1.790 ± 0.050	5437.570 W	3.000 ± 0.020	5436.586 W	7.530 ± 0.020	5435.39 A	3.510 ± 0.040
5445.853 M	6.246 ± 0.088	5439.46 A	1.770 ± 0.050	5439.580 A	2.870 ± 0.080	5437.487 A	7.500 ± 0.090	5435.41 W	3.480 ± 0.010
5447.924 M	6.249 ± 0.088	5440.45 A	1.770 ± 0.030	5441.957 M	2.900 ± 0.095	5437.570 W	7.470 ± 0.020	5436.32 W	3.470 ± 0.010
5449.974 M	6.213 ± 0.088	5440.46 W	1.770 ± 0.010	5443.945 M	3.075 ± 0.101	5440.570 W	7.480 ± 0.020	5436.36 A	3.490 ± 0.050
5450.470 A	5.980 ± 0.040	5440.95 M	1.736 ± 0.048	5444.520 A	3.040 ± 0.040	5442.003 M	7.227 ± 0.056	5437.33 W	3.460 ± 0.010
5451.769 M	6.065 ± 0.086	5441.91 M	1.752 ± 0.048	5445.480 A	2.980 ± 0.030	5442.959 M	7.199 ± 0.056	5437.37 A	3.500 ± 0.040
5452.470 A	5.770 ± 0.110	5442.29 W	1.840 ± 0.010	5446.980 M	3.026 ± 0.100	5443.412 A	7.180 ± 0.070	5438.30 A	3.440 ± 0.040
5453.838 M	6.025 ± 0.085	5442.90 M	1.776 ± 0.049	5447.500 W	3.140 ± 0.010	5443.539 W	7.020 ± 0.020	5438.38 W	3.460 ± 0.010
5454.450 A	5.840 ± 0.050	5443.36 W	1.760 ± 0.010	5447.530 A	3.000 ± 0.030	5443.558 C	7.082 ± 0.125	5439.27 W	3.420 ± 0.010
5454.786 M	5.935 ± 0.084	5443.38 A	1.790 ± 0.020	5447.969 M	3.014 ± 0.099	5444.407 A	7.120 ± 0.070	5439.41 A	3.370 ± 0.050
5455.440 A	5.840 ± 0.050	5443.51 C	1.725 ± 0.036	5448.560 A	2.970 ± 0.030	5444.960 M	7.072 ± 0.055	5440.35 W	3.440 ± 0.010
5456.460 A	5.880 ± 0.050	5444.31 W	1.750 ± 0.010	5450.580 A	3.120 ± 0.030	5446.527 W	7.150 ± 0.010	5440.36 A	3.380 ± 0.030
5456.893 M	5.899 ± 0.083	5444.38 A	1.770 ± 0.020	5451.580 A	3.090 ± 0.030	5447.555 W	7.000 ± 0.010	5441.40 W	3.440 ± 0.010
5457.770 M	5.952 ± 0.084	5444.46 C	1.702 ± 0.035	5452.958 M	3.037 ± 0.100	5447.579 A	6.970 ± 0.070	5441.73 M	3.455 ± 0.039
5458.844 M	5.994 ± 0.085	5444.89 M	1.726 ± 0.048	5454.540 A	3.120 ± 0.030	5449.571 A	7.160 ± 0.100	5442.27 W	3.460 ± 0.010
5459.440 A	5.790 ± 0.080	5445.39 A	1.760 ± 0.020	5454.900 M	3.026 ± 0.100	5450.504 C	6.988 ± 0.124	5442.71 M	3.447 ± 0.039
5463.360 A	5.860 ± 0.120	5446.52 W	1.710 ± 0.010	5455.580 A	3.110 ± 0.030	5450.544 A	7.070 ± 0.060	5443.32 A	3.430 ± 0.030
5466.850 M	6.106 ± 0.086	5446.93 M	1.744 ± 0.048	5455.888 M	3.064 ± 0.101	5450.962 M	6.997 ± 0.055	5443.34 W	3.430 ± 0.010
5467.895 M	5.999 ± 0.085	5447.33 W	1.750 ± 0.010	5456.517 C	3.131 ± 0.100	5451.498 C	7.161 ± 0.127	5443.43 C	3.448 ± 0.075
5468.846 M	5.958 ± 0.084	5447.49 A	1.780 ± 0.020	5456.570 A	3.120 ± 0.040	5453.980 M	7.169 ± 0.056	5443.76 M	3.459 ± 0.039
5469.827 M	6.102 ± 0.086	5448.33 W	1.730 ± 0.010	5457.490 C	3.182 ± 0.102	5454.509 A	7.080 ± 0.080	5444.27 W	3.440 ± 0.010
5470.913 M	6.286 ± 0.089	5448.46 A	1.750 ± 0.020	5457.520 A	3.120 ± 0.040	5454.975 M	7.179 ± 0.056	5444.32 A	3.470 ± 0.030
5472.906 M	6.272 ± 0.088	5449.33 W	1.720 ± 0.010	5457.901 M	3.077 ± 0.101	5455.553 A	7.180 ± 0.080	5444.38 C	3.351 ± 0.073
5473.848 M	6.234 ± 0.088	5449.54 A	1.750 ± 0.020	5458.505 C	3.281 ± 0.105	5455.978 M	7.250 ± 0.057	5444.71 M	3.455 ± 0.039
5476.795 M	6.445 ± 0.091	5449.90 M	1.803 ± 0.050	5458.530 A	3.140 ± 0.040	5456.408 C	7.012 ± 0.124	5445.26 A	3.410 ± 0.030
5477.770 M	6.388 ± 0.090	5450.29 W	1.710 ± 0.010	5458.957 M	3.085 ± 0.101	5456.543 A	7.400 ± 0.080	5445.73 M	3.453 ± 0.039
5478.905 M	6.450 ± 0.091	5450.44 A	1.730 ± 0.020	5459.521 C	3.144 ± 0.100	5456.968 M	7.316 ± 0.057	5446.41 W	3.450 ± 0.010
5479.759 M	6.414 ± 0.090	5450.90 M	1.793 ± 0.049	5459.530 A	3.190 ± 0.030	5457.412 C	7.169 ± 0.127	5446.73 M	3.482 ± 0.039
5480.828 M	6.487 ± 0.091	5451.45 C	1.675 ± 0.035	5460.500 W	3.320 ± 0.010	5457.459 A	7.420 ± 0.080	5447.36 A	3.450 ± 0.030
5481.809 M	6.537 ± 0.092	5451.50 A	1.750 ± 0.020	5460.560 A	3.250 ± 0.040	5457.968 M	7.379 ± 0.058	5447.49 W	3.440 ± 0.010
5482.786 M	6.555 ± 0.092	5451.84 M	1.712 ± 0.047	5461.520 W	3.430 ± 0.020	5458.501 A	7.480 ± 0.080	5447.65 M	3.445 ± 0.039
5483.779 M	6.482 ± 0.091	5452.44 A	1.710 ± 0.020	5462.530 A	3.310 ± 0.050	5458.544 C	7.472 ± 0.132	5448.31 W	3.430 ± 0.010
5486.777 M	6.640 ± 0.094	5452.44 C	1.683 ± 0.035	5463.440 W	3.430 ± 0.010	5459.484 C	7.434 ± 0.132	5448.34 A	3.450 ± 0.030
5488.789 M	6.658 ± 0.094	5453.53 A	1.700 ± 0.030	5463.530 A	3.320 ± 0.060	5459.506 A	7.550 ± 0.090	5449.28 W	3.400 ± 0.010
5497.755 M	6.922 ± 0.098	5453.89 M	1.731 ± 0.048	5464.520 A	3.420 ± 0.050	5460.511 A	7.690 ± 0.120	5449.34 A	3.420 ± 0.030
5498.767 M	6.823 ± 0.096	5454.31 W	1.670 ± 0.010	5465.460 W	3.200 ± 0.030	5460.512 W	7.530 ± 0.020	5449.71 M	3.374 ± 0.038
5499.751 M	6.774 ± 0.096	5454.39 C	1.699 ± 0.035	5465.570 A	3.310 ± 0.070	5461.492 W	7.440 ± 0.020	5450.27 W	3.350 ± 0.010
5500.767 M	6.929 ± 0.098	5454.43 A	1.700 ± 0.020	5466.896 M	3.481 ± 0.115	5462.590 A	7.720 ± 0.080	5450.33 A	3.350 ± 0.020
5501.757 M	7.226 ± 0.102	5454.84 M	1.666 ± 0.046	5468.580 A	3.450 ± 0.100	5463.461 W	7.370 ± 0.020	5450.71 M	3.322 ± 0.038
5502.784 M	7.273 ± 0.103	5455.41 A	1.670 ± 0.010	5470.540 W	3.730 ± 0.010	5463.492 A	7.740 ± 0.110	5451.36 C	3.340 ± 0.072
5503.766 M	7.440 ± 0.105	5455.83 M	1.658 ± 0.046	5470.971 M	3.910 ± 0.129	5463.946 M	7.840 ± 0.061	5451.39 A	3.350 ± 0.030
5504.370 A	7.680 ± 0.060	5456.37 C	1.635 ± 0.034	5471.450 W	3.870 ± 0.010	5464.442 A	7.870 ± 0.100	5451.64 M	3.358 ± 0.038
5504.795 M	7.625 ± 0.108	5456.43 A	1.690 ± 0.020	5471.923 M	3.779 ± 0.124	5465.457 W	7.680 ± 0.030	5452.29 W	3.330 ± 0.010
5505.768 M	7.710 ± 0.109	5457.38 C	1.667 ± 0.034	5472.967 M	4.012 ± 0.132	5465.607 A	7.800 ± 0.140	5452.34 C	3.265 ± 0.071
5506.763 M	7.740 ± 0.109	5457.44 A	1.690 ± 0.020	5473.550 W	3.910 ± 0.010	5466.961 M	7.847 ± 0.061	5452.35 A	3.330 ± 0.020
5507.779 M	7.895 ± 0.111	5457.84 M	1.637 ± 0.045	5476.917 M	3.955 ± 0.130	5467.484 W	7.760 ± 0.020	5453.36 A	3.270 ± 0.030
5508.766 M	7.944 ± 0.112	5458.30 W	1.660 ± 0.010	5477.905 M	3.782 ± 0.124	5467.974 M	7.924 ± 0.062	5453.70 M	3.322 ± 0.038
5509.404 C	8.229 ± 0.095	5458.47 A	1.640 ± 0.020	5479.510 W	4.020 ± 0.010	5468.429 C	7.728 ± 0.137	5454.26 W	3.300 ± 0.010
5510.734 M	8.038 ± 0.113	5458.47 C	1.615 ± 0.033	5479.896 M	3.964 ± 0.130	5468.539 W	7.910 ± 0.020	5454.32 A	3.280 ± 0.030
5511.270 W	7.980 ± 0.020	5458.90 M	1.661 ± 0.046	5480.882 M	3.820 ± 0.126	5468.988 M	7.784 ± 0.061	5454.34 C	3.258 ± 0.071
5513.300 W	8.750 ± 0.020	5459.29 W	1.630 ± 0.010	5481.924 M	4.240 ± 0.139	5469.496 W	7.870 ± 0.020	5454.64 M	3.312 ± 0.037
5513.718 M	8.735 ± 0.123	5459.41 A	1.710 ± 0.040	5482.520 W	4.010 ± 0.010	5470.523 W	7.820 ± 0.020	5455.32 A	3.310 ± 0.030
5514.280 W	8.790 ± 0.020	5460.34 W	1.630 ± 0.010	5482.540 C	3.921 ± 0.125	5471.492 W	7.780 ± 0.010	5456.28 C	3.251 ± 0.071
5514.716 M	8.825 ± 0.124	5462.36 A	1.480 ± 0.050	5482.560 A	4.110 ± 0.040	5471.987 M	8.037 ± 0.063	5456.33 A	3.310 ± 0.030
5515.360 W	8.970 ± 0.030	5465.45 A	1.610 ± 0.040	5482.912 M	3.966 ± 0.130	5473.566 W	8.010 ± 0.010	5456.69 M	3.281 ± 0.037
5515.364 C	8.951 ± 0.104	5466.27 W	1.520 ± 0.020	5483.520 W	4.190 ± 0.010	5474.453 W	8.230 ± 0.010	5457.27 A	3.290 ± 0.030
5515.722 M	9.043 ± 0.128	5466.44 A	1.600 ± 0.040	5483.528 C	4.128 ± 0.132	5476.973 M	8.194 ± 0.064	5457.29 C	3.228 ± 0.070
5516.250 A	8.730 ± 0.080	5467.27 W	1.540 ± 0.010	5483.590 A	4.150 ± 0.040	5477.971 M	8.140 ± 0.063	5457.64 M	3.295 ± 0.037
5516.721 M	8.931 ± 0.126	5468.38 C	1.514 ± 0.031	5483.887 M	4.064 ± 0.134	5478.960 M	8.304 ± 0.065	5458.30 W	3.340 ± 0.060

Table 5
(Continued)

Mrk 335		Mrk 1501		3C 120		Mrk 6		PG 2130+099	
HJD[a]	F_{con}[b]	HJD[a]	F_{con}[b]	HJD[a]	F_{con}[b]	HJD[a]	F_{con}[b]	HJD[a]	F_{con}[b]
5517.310 A	8.940 ± 0.110	5468.44 A	1.570 ± 0.020	5484.470 A	4.120 ± 0.120	5479.484 W	8.390 ± 0.010	5458.30 A	3.190 ± 0.010
5517.384 C	8.944 ± 0.104	5468.49 W	1.540 ± 0.010	5484.490 W	4.010 ± 0.010	5479.960 M	8.304 ± 0.065	5459.32 A	3.320 ± 0.090
5517.714 M	8.931 ± 0.126	5468.87 M	1.616 ± 0.045	5485.490 A	4.190 ± 0.050	5480.945 M	8.464 ± 0.066	5460.35 A	3.430 ± 0.110
5518.280 A	8.700 ± 0.130	5469.31 W	1.520 ± 0.010	5485.510 W	4.000 ± 0.010	5481.980 M	8.496 ± 0.066	5462.27 A	3.210 ± 0.050
5518.412 C	8.638 ± 0.100	5469.89 M	1.538 ± 0.042	5485.946 M	4.141 ± 0.136	5482.480 W	8.510 ± 0.020	5463.29 A	3.310 ± 0.060
5518.711 M	8.644 ± 0.122	5470.38 W	1.500 ± 0.010	5486.350 W	4.220 ± 0.010	5482.502 C	8.478 ± 0.150	5463.33 W	3.140 ± 0.020
5519.715 M	8.747 ± 0.123	5471.38 W	1.510 ± 0.010	5486.897 M	4.135 ± 0.136	5482.594 A	8.290 ± 0.080	5464.28 A	3.270 ± 0.040
5520.727 M	8.790 ± 0.124	5471.49 A	1.530 ± 0.020	5487.922 M	4.278 ± 0.141	5482.979 M	8.466 ± 0.066	5465.27 A	3.160 ± 0.040
5521.170 W	8.560 ± 0.030	5472.27 W	1.500 ± 0.010	5488.510 W	4.150 ± 0.010	5483.504 W	8.360 ± 0.010	5465.32 W	3.150 ± 0.010
5521.734 M	8.715 ± 0.123	5473.30 W	1.490 ± 0.010	5488.925 M	4.138 ± 0.136	5483.568 C	8.604 ± 0.152	5466.25 W	3.190 ± 0.010
5523.230 W	8.280 ± 0.030	5474.44 W	1.490 ± 0.010	5489.480 W	4.090 ± 0.010	5483.617 A	8.410 ± 0.090	5467.35 W	3.210 ± 0.010
5523.290 A	8.360 ± 0.100	5475.39 A	1.500 ± 0.020	5490.490 A	4.180 ± 0.050	5484.469 W	8.420 ± 0.010	5468.27 C	3.185 ± 0.069
5524.390 W	8.530 ± 0.030	5476.28 W	1.480 ± 0.010	5492.460 A	4.150 ± 0.060	5485.418 W	8.520 ± 0.010	5468.32 A	3.280 ± 0.020
5525.280 A	8.130 ± 0.140	5476.86 M	1.474 ± 0.041	5493.490 A	4.110 ± 0.090	5486.469 W	8.450 ± 0.010	5468.34 W	3.240 ± 0.010
5525.320 W	8.170 ± 0.020	5477.31 W	1.440 ± 0.010	5494.550 A	3.960 ± 0.080	5486.979 M	8.580 ± 0.067	5469.32 W	3.300 ± 0.010
5525.703 M	8.168 ± 0.115	5477.83 M	1.430 ± 0.039	5495.530 A	4.060 ± 0.160	5487.983 M	8.716 ± 0.068	5470.33 W	3.320 ± 0.010
5526.290 W	8.010 ± 0.020	5478.22 W	1.410 ± 0.010	5496.890 M	3.940 ± 0.130	5488.516 W	8.590 ± 0.010	5470.71 M	3.252 ± 0.037
5526.707 M	8.161 ± 0.115	5479.32 W	1.440 ± 0.010	5497.480 W	4.140 ± 0.020	5488.965 M	8.865 ± 0.069	5471.30 A	3.350 ± 0.030
5527.240 W	7.960 ± 0.020	5479.84 M	1.429 ± 0.039	5497.882 M	3.815 ± 0.126	5489.461 W	8.700 ± 0.020	5471.41 W	3.340 ± 0.010
5527.742 M	8.020 ± 0.113	5481.23 W	1.440 ± 0.010	5499.869 M	3.826 ± 0.126	5490.426 W	8.820 ± 0.020	5472.42 W	3.360 ± 0.010
5528.250 W	7.970 ± 0.020	5481.87 M	1.437 ± 0.040	5500.540 A	3.980 ± 0.040	5492.531 A	9.130 ± 0.100	5472.77 M	3.322 ± 0.038
5528.713 M	8.081 ± 0.114	5482.29 W	1.430 ± 0.010	5500.887 M	3.766 ± 0.124	5493.529 A	9.400 ± 0.130	5473.23 W	3.360 ± 0.010
5529.340 W	8.230 ± 0.020	5482.40 A	1.490 ± 0.010	5501.450 A	3.950 ± 0.050	5493.997 M	9.358 ± 0.073	5473.66 M	3.333 ± 0.038
5529.727 M	7.936 ± 0.112	5482.42 C	1.434 ± 0.030	5501.487 C	3.920 ± 0.125	5494.575 A	9.230 ± 0.110	5474.42 W	3.300 ± 0.010
5530.713 M	8.072 ± 0.114	5482.85 M	1.420 ± 0.039	5501.887 M	3.944 ± 0.130	5495.573 A	9.270 ± 0.150	5474.70 M	3.335 ± 0.038
5531.708 M	7.691 ± 0.108	5483.43 A	1.430 ± 0.020	5502.500 A	4.020 ± 0.040	5496.954 M	9.466 ± 0.074	5475.25 A	3.340 ± 0.020
5532.240 W	7.570 ± 0.020	5483.48 W	1.440 ± 0.010	5502.908 M	3.789 ± 0.125	5497.512 W	9.380 ± 0.020	5476.20 W	3.320 ± 0.010
5532.720 M	7.621 ± 0.107	5483.49 C	1.464 ± 0.030	5503.500 A	3.880 ± 0.040	5497.947 M	9.504 ± 0.074	5477.35 W	3.310 ± 0.010
5533.779 M	7.750 ± 0.109	5483.85 M	1.389 ± 0.038	5503.560 W	3.900 ± 0.010	5498.950 M	9.547 ± 0.074	5477.64 M	3.292 ± 0.037
5534.270 W	7.400 ± 0.020	5484.31 W	1.430 ± 0.010	5503.908 M	4.086 ± 0.134	5499.932 M	9.685 ± 0.076	5478.64 M	3.295 ± 0.037
5535.260 W	7.570 ± 0.020	5484.36 A	1.520 ± 0.040	5504.360 W	3.950 ± 0.010	5500.499 C	9.855 ± 0.174	5479.40 W	3.310 ± 0.010
5535.330 A	7.650 ± 0.050	5485.31 W	1.450 ± 0.010	5504.410 A	3.890 ± 0.030	5500.587 A	9.710 ± 0.110	5480.63 M	3.275 ± 0.037
5536.782 M	7.564 ± 0.107	5485.39 A	1.470 ± 0.020	5504.915 M	3.655 ± 0.120	5500.958 M	9.743 ± 0.076	5481.18 W	3.330 ± 0.010
5537.343 C	7.747 ± 0.090	5486.29 W	1.430 ± 0.010	5505.340 W	3.850 ± 0.010	5501.534 A	9.610 ± 0.120	5481.62 M	3.276 ± 0.037
5537.360 W	7.620 ± 0.020	5486.84 M	1.451 ± 0.040	5505.500 A	3.800 ± 0.040	5501.556 C	9.716 ± 0.172	5482.28 A	3.330 ± 0.030
5537.760 M	7.560 ± 0.107	5488.50 W	1.440 ± 0.010	5505.892 M	3.674 ± 0.121	5501.955 M	9.753 ± 0.076	5482.32 C	3.187 ± 0.069
5538.180 W	7.440 ± 0.020	5489.29 W	1.370 ± 0.010	5506.460 A	3.760 ± 0.040	5502.555 A	9.680 ± 0.090	5482.32 W	3.310 ± 0.010
5538.270 A	7.660 ± 0.060	5492.41 A	1.460 ± 0.040	5506.550 W	3.770 ± 0.010	5502.976 M	9.703 ± 0.076	5482.62 M	3.343 ± 0.038
5538.767 M	7.614 ± 0.107	5493.20 W	1.420 ± 0.020	5506.888 M	3.555 ± 0.117	5503.539 W	9.690 ± 0.020	5483.29 W	3.280 ± 0.010
5539.280 A	7.780 ± 0.060	5493.37 A	1.470 ± 0.030	5507.380 W	3.810 ± 0.010	5503.563 A	9.700 ± 0.140	5483.30 A	3.320 ± 0.030
5539.284 C	7.624 ± 0.088	5494.42 A	1.510 ± 0.030	5507.490 A	3.780 ± 0.030	5503.973 M	9.767 ± 0.076	5483.37 C	3.348 ± 0.073
5539.762 M	7.724 ± 0.109	5495.23 W	1.430 ± 0.010	5507.895 M	3.728 ± 0.123	5504.391 W	9.700 ± 0.020	5484.27 A	3.300 ± 0.030
5540.763 M	7.763 ± 0.109	5495.48 A	1.490 ± 0.060	5508.300 W	3.600 ± 0.010	5504.552 A	9.680 ± 0.130	5484.29 W	3.290 ± 0.010
5541.220 W	7.420 ± 0.020	5497.37 W	1.420 ± 0.010	5508.420 A	3.780 ± 0.040	5504.981 M	9.690 ± 0.076	5485.30 W	3.300 ± 0.010
5541.764 M	7.721 ± 0.109	5497.83 M	1.430 ± 0.039	5508.526 C	3.694 ± 0.118	5505.352 W	9.640 ± 0.020	5486.25 A	3.310 ± 0.040
5542.755 M	8.013 ± 0.113	5498.25 W	1.420 ± 0.010	5508.897 M	3.684 ± 0.121	5505.546 A	9.650 ± 0.090	5486.30 W	3.200 ± 0.010
5543.759 M	8.013 ± 0.113	5498.36 A	1.460 ± 0.030	5509.450 W	3.750 ± 0.010	5505.957 M	9.687 ± 0.076	5488.27 W	3.040 ± 0.020
5544.724 M	7.982 ± 0.113	5498.83 M	1.445 ± 0.040	5509.505 C	3.766 ± 0.120	5506.484 A	9.890 ± 0.090	5488.62 M	3.217 ± 0.036
5545.310 W	8.230 ± 0.030	5499.81 M	1.450 ± 0.040	5509.510 A	3.740 ± 0.040	5506.500 W	9.680 ± 0.020	5489.39 W	3.100 ± 0.020
5545.732 M	8.190 ± 0.115	5500.35 A	1.460 ± 0.010	5510.490 A	3.670 ± 0.040	5506.951 M	9.720 ± 0.076	5490.29 W	3.130 ± 0.020
5546.734 M	8.413 ± 0.119	5500.83 M	1.486 ± 0.041	5510.864 M	3.792 ± 0.125	5507.383 W	9.650 ± 0.020	5491.27 W	3.230 ± 0.010
5549.240 A	8.230 ± 0.230	5501.29 A	1.440 ± 0.010	5511.480 A	3.660 ± 0.040	5507.540 A	9.700 ± 0.090	5492.16 W	3.160 ± 0.020
5549.606 M	8.113 ± 0.114	5501.43 C	1.488 ± 0.031	5511.861 M	3.710 ± 0.122	5507.959 M	9.738 ± 0.076	5492.24 A	3.180 ± 0.040
5550.671 M	8.375 ± 0.118	5501.83 M	1.438 ± 0.040	5512.450 A	3.670 ± 0.040	5508.553 A	9.710 ± 0.100	5493.17 W	3.180 ± 0.010
5553.260 A	8.250 ± 0.080	5502.22 W	1.440 ± 0.010	5512.837 M	3.400 ± 0.112	5508.589 C	9.486 ± 0.168	5493.27 A	3.260 ± 0.050
5554.280 A	8.390 ± 0.060	5502.33 A	1.480 ± 0.010	5513.440 W	3.670 ± 0.010	5508.960 M	9.659 ± 0.075	5493.61 M	3.204 ± 0.036
5555.713 M	8.464 ± 0.119	5502.85 M	1.480 ± 0.041	5513.841 M	3.629 ± 0.119	5509.430 W	9.620 ± 0.020	5494.21 A	3.200 ± 0.040
5556.230 A	8.340 ± 0.080	5503.26 W	1.460 ± 0.010	5514.410 W	3.770 ± 0.010	5509.540 A	9.540 ± 0.090	5495.17 W	3.140 ± 0.010
5556.720 M	8.279 ± 0.117	5503.34 A	1.460 ± 0.020	5514.450 A	3.690 ± 0.040	5509.568 C	9.725 ± 0.172	5496.17 W	3.140 ± 0.010
5557.716 M	8.334 ± 0.118	5503.85 M	1.429 ± 0.039	5514.835 M	3.818 ± 0.126	5510.542 A	9.490 ± 0.070	5496.60 M	3.082 ± 0.035
5559.711 M	8.526 ± 0.120	5504.25 W	1.460 ± 0.010	5515.370 W	3.690 ± 0.010	5510.931 M	9.570 ± 0.075	5497.27 W	3.110 ± 0.010
5568.240 A	8.420 ± 0.070	5504.27 A	1.440 ± 0.020	5515.425 C	3.697 ± 0.118	5511.530 A	9.430 ± 0.100	5497.60 M	3.106 ± 0.035
5568.247 C	8.614 ± 0.100	5504.85 M	1.414 ± 0.039	5515.470 A	3.630 ± 0.040	5511.923 M	9.366 ± 0.073	5498.23 W	3.100 ± 0.010
5569.240 A	8.430 ± 0.060	5505.23 W	1.430 ± 0.010	5515.844 M	3.744 ± 0.123	5512.899 M	9.305 ± 0.073	5498.25 A	3.090 ± 0.020
		5505.35 A	1.430 ± 0.010	5516.330 W	3.550 ± 0.010	5513.473 W	9.290 ± 0.020	5498.61 M	3.080 ± 0.035

Table 5
(Continued)

Mrk 335		Mrk 1501		3C 120		Mrk 6		PG 2130+099	
HJD[a]	F_{con}[b]	HJD[a]	F_{con}[b]	HJD[a]	F_{con}[b]	HJD[a]	F_{con}[b]	HJD[a]	F_{con}[b]
		5505.83 M	1.406 ± 0.039	5516.440 A	3.660 ± 0.040	5513.902 M	9.239 ± 0.072	5499.25 A	3.090 ± 0.030
		5506.30 W	1.420 ± 0.010	5516.497 C	3.463 ± 0.110	5514.422 W	9.280 ± 0.020	5499.60 M	3.035 ± 0.034
		5506.32 A	1.440 ± 0.020	5516.843 M	3.677 ± 0.121	5514.471 A	9.430 ± 0.080	5500.26 A	3.070 ± 0.020
		5506.83 M	1.435 ± 0.040	5517.460 A	3.680 ± 0.040	5514.897 M	9.212 ± 0.072	5500.29 C	3.052 ± 0.066
		5507.33 W	1.410 ± 0.010	5517.490 C	3.729 ± 0.119	5515.359 W	9.230 ± 0.020	5500.61 M	3.013 ± 0.034
		5507.35 A	1.390 ± 0.010	5517.847 M	3.600 ± 0.118	5515.555 A	9.380 ± 0.090	5501.30 C	2.999 ± 0.065
		5507.83 M	1.378 ± 0.038	5518.450 A	3.570 ± 0.060	5515.571 C	9.163 ± 0.162	5501.60 M	2.945 ± 0.033
		5508.29 W	1.420 ± 0.010	5518.507 C	3.521 ± 0.112	5515.908 M	9.218 ± 0.072	5502.19 W	2.970 ± 0.010
		5508.34 A	1.420 ± 0.010	5519.470 A	3.430 ± 0.120	5516.344 W	9.310 ± 0.020	5502.25 A	2.990 ± 0.020
		5508.39 C	1.387 ± 0.029	5519.530 W	3.680 ± 0.020	5516.516 A	9.230 ± 0.100	5502.62 M	2.950 ± 0.033
		5508.82 M	1.429 ± 0.039	5519.858 M	3.747 ± 0.123	5516.539 C	9.397 ± 0.166	5503.22 W	2.920 ± 0.010
		5509.36 A	1.410 ± 0.020	5520.450 A	3.530 ± 0.070	5516.910 M	9.191 ± 0.072	5503.27 A	2.960 ± 0.040
		5509.36 C	1.386 ± 0.029	5525.530 W	3.500 ± 0.020	5517.543 C	9.011 ± 0.160	5503.61 M	2.884 ± 0.033
		5509.38 W	1.390 ± 0.010	5525.905 M	3.668 ± 0.121	5517.545 A	9.170 ± 0.080	5504.25 W	2.870 ± 0.010
		5510.81 M	1.397 ± 0.039	5526.350 W	3.280 ± 0.010	5517.913 M	9.123 ± 0.071	5504.31 A	2.850 ± 0.030
		5511.21 W	1.360 ± 0.010	5526.527 C	3.249 ± 0.104	5518.542 A	9.080 ± 0.100	5504.62 M	2.873 ± 0.032
		5511.32 A	1.380 ± 0.020	5526.833 M	3.570 ± 0.117	5518.564 C	9.429 ± 0.167	5505.28 A	2.830 ± 0.020
		5511.80 M	1.360 ± 0.038	5527.450 W	3.460 ± 0.010	5518.900 M	9.201 ± 0.072	5505.31 W	2.840 ± 0.010
		5512.33 A	1.380 ± 0.020	5527.854 M	3.594 ± 0.118	5519.484 W	9.280 ± 0.020	5505.61 M	2.836 ± 0.032
		5512.75 M	1.315 ± 0.036	5528.260 W	3.330 ± 0.010	5519.919 M	9.217 ± 0.072	5506.23 A	2.860 ± 0.020
		5513.40 W	1.360 ± 0.010	5528.848 M	3.432 ± 0.113	5520.501 A	9.100 ± 0.110	5506.25 W	2.830 ± 0.010
		5513.78 M	1.424 ± 0.039	5529.846 M	3.484 ± 0.115	5521.492 W	9.320 ± 0.020	5506.61 M	2.830 ± 0.032
		5514.30 A	1.350 ± 0.020	5530.310 W	3.380 ± 0.010	5523.908 M	9.436 ± 0.074	5507.24 A	2.850 ± 0.020
		5514.41 W	1.360 ± 0.010	5530.843 M	3.603 ± 0.119	5524.406 W	9.520 ± 0.030	5507.29 W	2.840 ± 0.010
		5514.78 M	1.400 ± 0.039	5531.290 W	3.290 ± 0.010	5525.445 W	9.340 ± 0.020	5507.62 M	2.761 ± 0.031
		5515.33 A	1.300 ± 0.020	5531.843 M	3.303 ± 0.109	5526.340 W	9.360 ± 0.020	5508.16 W	2.810 ± 0.010
		5515.33 C	1.335 ± 0.028	5532.320 W	3.350 ± 0.010	5526.592 C	9.636 ± 0.171	5508.25 A	2.790 ± 0.030
		5515.35 W	1.250 ± 0.010	5532.836 M	3.207 ± 0.106	5526.896 M	9.571 ± 0.075	5508.33 C	2.809 ± 0.061
		5515.79 M	1.367 ± 0.038	5533.850 M	3.195 ± 0.105	5527.410 W	9.470 ± 0.020	5508.61 M	2.760 ± 0.031
		5516.34 A	1.340 ± 0.020	5534.280 W	3.310 ± 0.010	5527.918 M	9.635 ± 0.075	5509.22 A	2.850 ± 0.020
		5517.34 A	1.350 ± 0.050	5535.280 W	3.260 ± 0.010	5528.911 M	9.739 ± 0.076	5509.23 C	2.887 ± 0.063
		5520.34 A	1.280 ± 0.030	5535.410 A	3.210 ± 0.040	5529.915 M	9.782 ± 0.076	5509.27 W	2.830 ± 0.010
		5523.23 W	1.260 ± 0.010	5535.825 M	3.118 ± 0.103	5530.324 W	9.980 ± 0.020	5509.62 M	2.792 ± 0.032
		5524.39 W	1.300 ± 0.010	5536.843 M	3.118 ± 0.103	5530.903 M	9.908 ± 0.077	5510.30 A	2.860 ± 0.040
		5525.34 W	1.270 ± 0.010	5537.440 W	3.190 ± 0.010	5531.297 W	9.850 ± 0.020	5510.62 M	2.846 ± 0.032
		5526.29 W	1.260 ± 0.010	5537.838 M	3.068 ± 0.101	5531.908 M	10.040 ± 0.078	5511.16 W	2.810 ± 0.010
		5526.79 M	1.256 ± 0.035	5538.410 A	3.160 ± 0.030	5532.441 W	9.980 ± 0.020	5511.18 A	2.840 ± 0.030
		5527.26 W	1.260 ± 0.010	5538.838 M	3.078 ± 0.101	5532.898 M	10.020 ± 0.078	5511.62 M	2.822 ± 0.032
		5527.78 M	1.341 ± 0.037	5539.366 C	3.179 ± 0.101	5533.914 M	10.070 ± 0.079	5512.26 A	2.850 ± 0.030
		5528.25 W	1.270 ± 0.010	5539.390 A	3.120 ± 0.030	5534.320 W	10.130 ± 0.020	5512.62 M	2.886 ± 0.033
		5528.79 M	1.402 ± 0.039	5539.832 M	3.038 ± 0.100	5534.507 A	10.170 ± 0.090	5513.22 A	2.940 ± 0.050
		5529.77 M	1.307 ± 0.036	5540.842 M	3.051 ± 0.100	5535.526 A	10.150 ± 0.070	5513.61 M	2.961 ± 0.033
		5530.78 M	1.258 ± 0.035	5541.260 W	3.130 ± 0.010	5535.888 M	10.110 ± 0.079	5514.21 A	2.930 ± 0.030
		5531.22 W	1.250 ± 0.010	5541.830 M	3.056 ± 0.101	5536.911 M	10.300 ± 0.080	5514.61 M	2.940 ± 0.033
		5531.77 M	1.279 ± 0.035	5542.869 M	3.189 ± 0.105	5537.465 W	10.230 ± 0.020	5515.19 C	2.977 ± 0.065
		5532.36 W	1.250 ± 0.010	5543.380 A	3.100 ± 0.040	5537.909 M	10.250 ± 0.080	5515.21 A	3.010 ± 0.030
		5532.77 M	1.248 ± 0.034	5543.827 M	3.106 ± 0.102	5538.478 C	10.269 ± 0.182	5515.62 M	2.951 ± 0.033
		5533.73 M	1.309 ± 0.036	5544.805 M	3.112 ± 0.102	5538.503 A	10.290 ± 0.100	5516.19 A	3.040 ± 0.030
		5534.25 A	1.270 ± 0.020	5545.340 W	3.200 ± 0.010	5538.898 M	10.230 ± 0.080	5516.26 C	3.016 ± 0.065
		5534.27 W	1.260 ± 0.010	5545.822 M	3.045 ± 0.100	5539.467 C	10.537 ± 0.187	5516.61 M	2.975 ± 0.034
		5535.30 W	1.270 ± 0.010	5546.841 M	3.309 ± 0.109	5539.513 A	10.230 ± 0.100	5517.26 A	2.930 ± 0.040
		5535.75 M	1.320 ± 0.036	5549.400 A	3.040 ± 0.090	5539.895 M	10.230 ± 0.080	5517.30 C	3.101 ± 0.067
		5536.73 M	1.281 ± 0.035	5549.793 M	3.158 ± 0.104	5540.905 M	10.270 ± 0.080	5517.61 M	2.930 ± 0.010
		5537.37 W	1.270 ± 0.010	5553.410 A	3.240 ± 0.060	5541.896 M	10.310 ± 0.080	5518.20 W	2.950 ± 0.040
		5537.67 M	1.266 ± 0.035	5554.380 A	3.150 ± 0.040	5542.891 M	10.410 ± 0.081	5518.21 A	3.124 ± 0.068
		5538.18 W	1.320 ± 0.010	5555.300 A	3.110 ± 0.070	5543.446 A	10.530 ± 0.100	5518.31 C	2.978 ± 0.034
		5538.29 A	1.260 ± 0.010	5557.796 M	3.408 ± 0.112	5543.895 M	10.440 ± 0.081	5519.27 A	2.940 ± 0.100
		5538.32 C	1.323 ± 0.027	5559.789 M	3.354 ± 0.110	5544.869 M	10.420 ± 0.081	5519.61 M	3.023 ± 0.034
		5538.71 M	1.288 ± 0.036	5566.370 A	3.700 ± 0.030	5545.328 W	10.660 ± 0.020	5520.19 W	3.000 ± 0.010
		5539.30 A	1.280 ± 0.010	5567.310 A	3.760 ± 0.030	5545.890 M	10.570 ± 0.082	5520.24 A	2.980 ± 0.030
		5539.31 C	1.307 ± 0.027	5568.350 A	3.750 ± 0.030	5546.946 M	10.580 ± 0.083	5521.15 W	3.010 ± 0.010
		5539.67 M	1.261 ± 0.035	5569.322 C	3.736 ± 0.119	5549.492 A	10.830 ± 0.140	5523.16 W	3.010 ± 0.010
		5540.72 M	1.310 ± 0.036			5549.869 M	10.730 ± 0.084	5523.20 A	2.970 ± 0.050
		5541.25 W	1.290 ± 0.010			5550.476 A	10.840 ± 0.120	5525.20 A	2.980 ± 0.030
		5541.71 M	1.351 ± 0.037			5550.856 M	10.890 ± 0.085	5525.24 W	2.970 ± 0.010

Table 5
(Continued)

Mrk 335		Mrk 1501		3C 120		Mrk 6		PG 2130+099	
HJD[a]	F_{con}[b]	HJD[a]	F_{con}[b]	HJD[a]	F_{con}[b]	HJD[a]	F_{con}[b]	HJD[a]	F_{con}[b]
		5542.70 M	1.341 ± 0.037			5553.448 A	10.700 ± 0.160	5525.24 C	2.946 ± 0.064
		5543.70 M	1.404 ± 0.039			5554.432 A	11.040 ± 0.110	5525.60 M	2.998 ± 0.034
		5546.68 M	1.430 ± 0.039			5555.324 A	11.620 ± 0.290	5526.24 W	2.990 ± 0.010
		5549.67 M	1.479 ± 0.041			5555.837 M	11.130 ± 0.087	5526.60 M	2.966 ± 0.034
		5550.67 M	1.437 ± 0.040			5556.859 M	10.940 ± 0.085	5527.22 W	2.940 ± 0.010
		5553.31 A	1.350 ± 0.030			5559.868 M	10.890 ± 0.085	5527.63 M	2.984 ± 0.034
		5554.32 A	1.390 ± 0.030			5566.428 A	11.040 ± 0.090	5528.24 W	2.930 ± 0.010
		5555.26 A	1.390 ± 0.030			5567.466 A	11.100 ± 0.080	5528.61 M	2.940 ± 0.033
		5556.67 M	1.398 ± 0.039			5569.399 A	10.910 ± 0.100	5529.61 M	2.958 ± 0.033
		5559.67 M	1.398 ± 0.039					5530.61 M	2.946 ± 0.033
		5568.21 C	1.415 ± 0.029					5531.18 W	2.890 ± 0.010
		5568.27 A	1.390 ± 0.010					5531.60 M	2.950 ± 0.033
								5532.20 W	2.890 ± 0.010
								5532.61 M	2.953 ± 0.033
								5533.61 M	2.930 ± 0.033
								5534.13 A	2.860 ± 0.060
								5534.20 W	2.890 ± 0.010
								5535.17 W	2.880 ± 0.010
								5536.61 M	2.908 ± 0.033
								5538.16 W	2.850 ± 0.010
								5538.17 C	2.962 ± 0.064
								5538.20 A	2.820 ± 0.020
								5538.61 M	2.874 ± 0.032
								5539.20 A	2.850 ± 0.020
								5539.22 C	2.874 ± 0.062
								5539.61 M	2.942 ± 0.033
								5540.60 M	2.909 ± 0.033
								5541.21 W	2.790 ± 0.010
								5541.57 M	2.921 ± 0.033
								5542.59 M	2.839 ± 0.032
								5543.60 M	2.920 ± 0.033
								5544.61 M	2.860 ± 0.032
								5548.61 M	2.862 ± 0.032
								5549.19 A	2.840 ± 0.040
								5551.18 A	2.930 ± 0.090
								5553.20 A	2.900 ± 0.050
								5555.20 A	2.910 ± 0.040
								5555.60 M	3.173 ± 0.036
								5556.19 A	2.960 ± 0.140
								5557.60 M	2.992 ± 0.034

Notes. Observatory code: C = CRAO Spectroscopy, A = CRAO Photometry, W = WISE, and M = MDM.
[a] Heliocentric Julian date (−2450000).
[b] Continuum fluxes are in units of 10^{-15} erg s^{-1} cm^{-2} Å^{-1}.

for all five objects. We list these in Table 8. The mean and variance of the light curve models calculated by SPEAR that are consistent with the data are shown in Figure 3. We also show the log-likelihood functions (log $(\mathscr{L}/\mathscr{L}_{max})$ as a function of τ) for these light curves in Figure 4. The likelihood $\mathscr{L}$ is defined in Equation (17) in Zu et al. (2011) and is proportional to $e^{-\chi^2/2}$. The best model, corresponding to $\mathscr{L}_{max}$, is associated with the minimum χ^2, χ^2_{min}. Thus, $\mathscr{L}/\mathscr{L}_{max} \propto e^{(-(\chi^2-\chi^2_{min})/2)}$ and $\Delta\chi^2 = -2\ln(\mathscr{L}/\mathscr{L}_{max})$. Therefore, Figure 4 effectively shows $\Delta\chi^2$ between models using each lag and the best model.

For comparison with previous results, we also include in Table 8 the lag measurements made using the interpolation method originally described by Gaskell & Sparke (1986) and Gaskell & Peterson (1987) which was later modified by White & Peterson (1994) and Peterson et al. (1998, 2004). We cross-correlate the continuum with the emission-line light curve, calculating the value of the cross-correlation coefficient r at each of many potential time lags. We show the CCFs for our light curves in Figure 4. Uncertainties in these lags are calculated using Monte Carlo simulations that employ the flux randomization and random subset selection methods of Peterson et al. (1998), as refined by Peterson et al. (2004). For each realization, we measure the lag ($\tau_{peak,CCF}$) that results in the peak value of the cross-correlation coefficient, r_{peak}. We also measure the lag at the centroid of the CCF ($\tau_{cent,CCF}$), calculated using points surrounding the peak with values greater than $0.8r_{peak}$. We adopt the mean of the distribution of delay measurements from our Monte Carlo realizations, and the standard deviations of the same distributions are adopted as our formal 1σ uncertainties. In the cases of Mrk 335, Mrk 6, and PG 2130+099, we subtracted linear trends before performing the CCF analysis, as there are clear secular trends in these light curves. This did not significantly affect the measured lag values, as can sometimes

Table 6
Hβ Fluxes

Mrk 335		Mrk1501		3C 120		Mrk 6		PG 2130+099	
HJD[a]	$F_{H\beta}$[b]	HJD[a]	$F_{H\beta}$[b]	HJD[a]	$F_{H\beta}$[b]	HJD[a]	$F_{H\beta}$[b]	HJD[a]	$F_{H\beta}$[b]
5440.908 M	5.323 ± 0.084	5440.934 M	2.453 ± 0.067	5441.957 M	3.368 ± 0.075	5442.003 M	6.213 ± 0.096	5441.725 M	4.385 ± 0.057
5441.869 M	5.496 ± 0.086	5441.893 M	2.546 ± 0.070	5443.945 M	3.502 ± 0.078	5442.959 M	6.129 ± 0.094	5442.714 M	4.334 ± 0.056
5442.838 M	5.296 ± 0.083	5442.873 M	2.537 ± 0.070	5446.980 M	3.438 ± 0.077	5443.558 C	6.389 ± 0.229	5443.430 C	4.377 ± 0.072
5444.840 M	5.287 ± 0.083	5443.516 C	2.404 ± 0.079	5447.969 M	3.373 ± 0.075	5444.960 M	6.144 ± 0.095	5443.764 M	4.300 ± 0.055
5445.853 M	5.217 ± 0.082	5444.465 C	2.459 ± 0.080	5452.958 M	3.308 ± 0.074	5450.504 C	6.210 ± 0.223	5444.384 C	4.291 ± 0.070
5447.924 M	5.264 ± 0.083	5444.870 M	2.517 ± 0.069	5454.900 M	3.309 ± 0.074	5450.962 M	6.017 ± 0.093	5444.714 M	4.391 ± 0.057
5449.974 M	5.565 ± 0.087	5446.904 M	2.508 ± 0.069	5455.888 M	3.375 ± 0.075	5451.498 C	6.118 ± 0.219	5445.727 M	4.393 ± 0.057
5451.769 M	5.470 ± 0.086	5449.879 M	2.583 ± 0.071	5456.517 C	3.319 ± 0.147	5453.979 M	6.040 ± 0.093	5446.725 M	4.303 ± 0.056
5453.838 M	5.458 ± 0.086	5450.873 M	2.522 ± 0.069	5457.490 C	3.395 ± 0.150	5454.974 M	5.829 ± 0.090	5447.648 M	4.341 ± 0.056
5454.786 M	5.441 ± 0.085	5451.458 C	2.452 ± 0.080	5457.901 M	3.418 ± 0.076	5455.977 M	5.936 ± 0.091	5449.711 M	4.366 ± 0.056
5456.893 M	5.362 ± 0.084	5451.810 M	2.570 ± 0.070	5458.505 C	3.597 ± 0.159	5456.408 C	6.025 ± 0.216	5450.705 M	4.313 ± 0.056
5457.770 M	5.509 ± 0.086	5452.442 C	2.520 ± 0.082	5458.957 M	3.388 ± 0.076	5456.968 M	5.991 ± 0.092	5451.357 C	4.318 ± 0.071
5458.844 M	5.324 ± 0.084	5453.867 M	2.523 ± 0.069	5459.521 C	3.442 ± 0.152	5457.412 C	6.060 ± 0.217	5451.638 M	4.316 ± 0.056
5466.850 M	5.122 ± 0.080	5454.398 C	2.414 ± 0.079	5466.896 M	3.609 ± 0.081	5457.967 M	5.886 ± 0.091	5452.336 C	4.391 ± 0.072
5467.895 M	5.200 ± 0.082	5454.813 M	2.447 ± 0.067	5470.971 M	3.557 ± 0.080	5458.544 C	6.028 ± 0.216	5453.699 M	4.404 ± 0.057
5468.846 M	4.976 ± 0.078	5455.804 M	2.459 ± 0.067	5471.923 M	3.496 ± 0.078	5459.484 C	6.081 ± 0.218	5454.337 C	4.357 ± 0.071
5469.827 M	5.062 ± 0.079	5456.373 C	2.448 ± 0.080	5472.967 M	3.599 ± 0.081	5463.946 M	6.042 ± 0.093	5454.639 M	4.377 ± 0.056
5470.913 M	5.087 ± 0.080	5457.385 C	2.465 ± 0.081	5476.917 M	3.507 ± 0.078	5466.960 M	6.084 ± 0.094	5456.280 C	4.218 ± 0.069
5472.906 M	5.042 ± 0.079	5457.815 M	2.375 ± 0.065	5477.905 M	3.410 ± 0.076	5467.973 M	5.949 ± 0.092	5456.692 M	4.343 ± 0.056
5473.848 M	4.979 ± 0.078	5458.475 C	2.447 ± 0.080	5479.896 M	3.541 ± 0.079	5468.429 C	6.178 ± 0.222	5457.290 C	4.272 ± 0.070
5476.795 M	5.218 ± 0.082	5458.871 M	2.414 ± 0.066	5480.882 M	3.463 ± 0.077	5468.988 M	5.941 ± 0.091	5457.637 M	4.239 ± 0.055
5477.770 M	5.081 ± 0.080	5468.384 C	2.305 ± 0.075	5481.924 M	3.785 ± 0.085	5471.986 M	6.088 ± 0.094	5468.275 C	4.310 ± 0.071
5478.905 M	5.037 ± 0.079	5468.874 M	2.495 ± 0.068	5482.540 C	3.580 ± 0.158	5476.973 M	6.283 ± 0.097	5470.707 M	4.337 ± 0.056
5479.759 M	5.063 ± 0.079	5469.857 M	2.448 ± 0.067	5482.912 M	3.560 ± 0.080	5477.970 M	6.425 ± 0.099	5472.766 M	4.276 ± 0.055
5480.828 M	5.069 ± 0.080	5476.828 M	2.483 ± 0.068	5483.528 C	3.581 ± 0.158	5478.960 M	6.277 ± 0.097	5473.661 M	4.255 ± 0.055
5481.809 M	5.075 ± 0.080	5477.801 M	2.294 ± 0.063	5483.887 M	3.541 ± 0.079	5479.959 M	6.359 ± 0.098	5474.705 M	4.320 ± 0.056
5482.786 M	5.235 ± 0.082	5479.808 M	2.235 ± 0.061	5485.946 M	3.684 ± 0.082	5480.945 M	6.275 ± 0.097	5477.641 M	4.274 ± 0.055
5483.779 M	5.097 ± 0.080	5481.837 M	2.319 ± 0.064	5486.897 M	3.656 ± 0.082	5481.979 M	6.163 ± 0.095	5478.640 M	4.304 ± 0.056
5486.777 M	5.261 ± 0.083	5482.424 C	2.248 ± 0.074	5487.922 M	3.715 ± 0.083	5482.502 C	6.245 ± 0.224	5480.633 M	4.286 ± 0.055
5488.789 M	5.243 ± 0.082	5482.825 M	2.181 ± 0.060	5488.925 M	3.706 ± 0.083	5482.979 M	6.310 ± 0.097	5481.625 M	4.290 ± 0.055
5497.755 M	5.278 ± 0.083	5483.491 C	2.096 ± 0.069	5496.890 M	3.832 ± 0.086	5483.568 C	6.469 ± 0.232	5482.315 C	4.361 ± 0.071
5498.767 M	5.307 ± 0.083	5483.816 M	2.216 ± 0.061	5497.882 M	3.737 ± 0.084	5486.979 M	6.518 ± 0.100	5482.624 M	4.328 ± 0.056
5499.751 M	5.323 ± 0.084	5486.810 M	2.260 ± 0.062	5499.869 M	3.818 ± 0.085	5487.983 M	6.392 ± 0.098	5483.367 C	4.285 ± 0.070
5500.767 M	5.386 ± 0.085	5497.794 M	2.091 ± 0.057	5500.887 M	3.717 ± 0.083	5488.965 M	6.726 ± 0.104	5488.624 M	4.229 ± 0.055
5501.757 M	5.258 ± 0.083	5498.800 M	2.187 ± 0.060	5501.487 C	3.859 ± 0.171	5493.996 M	6.556 ± 0.101	5493.612 M	4.334 ± 0.056
5502.784 M	5.257 ± 0.083	5499.782 M	2.057 ± 0.056	5501.887 M	3.845 ± 0.086	5496.954 M	6.657 ± 0.103	5496.602 M	4.334 ± 0.056
5503.766 M	5.324 ± 0.084	5500.800 M	2.219 ± 0.061	5502.908 M	3.797 ± 0.085	5497.947 M	6.959 ± 0.107	5497.599 M	4.231 ± 0.055
5504.795 M	5.300 ± 0.083	5501.431 C	2.150 ± 0.070	5503.908 M	3.932 ± 0.088	5498.949 M	6.959 ± 0.107	5498.608 M	4.315 ± 0.056
5505.768 M	5.353 ± 0.084	5501.787 M	2.064 ± 0.057	5504.915 M	3.768 ± 0.084	5499.931 M	6.894 ± 0.106	5499.599 M	4.349 ± 0.056
5506.763 M	5.403 ± 0.085	5502.827 M	2.069 ± 0.057	5505.892 M	3.700 ± 0.083	5500.499 C	6.693 ± 0.240	5500.286 C	4.200 ± 0.069
5507.779 M	5.385 ± 0.085	5503.816 M	2.047 ± 0.056	5506.888 M	3.798 ± 0.085	5500.957 M	7.135 ± 0.110	5500.612 M	4.212 ± 0.054
5508.766 M	5.397 ± 0.085	5504.825 M	2.072 ± 0.057	5507.895 M	3.891 ± 0.087	5501.556 C	7.130 ± 0.256	5501.295 C	4.127 ± 0.068
5509.404 C	5.667 ± 0.092	5505.803 M	2.108 ± 0.058	5508.526 C	4.113 ± 0.182	5501.955 M	7.021 ± 0.108	5501.600 M	4.278 ± 0.055
5510.734 M	5.662 ± 0.089	5506.797 M	2.091 ± 0.057	5508.897 M	3.962 ± 0.089	5502.976 M	7.182 ± 0.111	5502.616 M	4.321 ± 0.056
5513.718 M	5.485 ± 0.086	5507.803 M	2.064 ± 0.057	5509.505 C	4.078 ± 0.180	5503.972 M	7.088 ± 0.109	5503.608 M	4.293 ± 0.055
5514.716 M	5.678 ± 0.089	5508.396 C	2.129 ± 0.070	5510.864 M	4.131 ± 0.092	5504.981 M	7.226 ± 0.111	5504.616 M	4.271 ± 0.055
5515.364 C	5.845 ± 0.095	5508.790 M	2.057 ± 0.056	5511.861 M	4.014 ± 0.090	5505.957 M	7.127 ± 0.110	5505.612 M	4.293 ± 0.055
5515.722 M	5.776 ± 0.091	5509.367 C	2.118 ± 0.069	5512.837 M	3.883 ± 0.087	5506.951 M	7.365 ± 0.113	5506.608 M	4.242 ± 0.055
5516.721 M	5.907 ± 0.093	5510.772 M	2.019 ± 0.055	5513.841 M	4.027 ± 0.090	5507.959 M	7.331 ± 0.113	5507.624 M	4.204 ± 0.054
5517.384 C	5.749 ± 0.094	5511.773 M	2.010 ± 0.055	5514.835 M	4.100 ± 0.092	5508.589 C	7.502 ± 0.269	5508.325 C	4.150 ± 0.068
5517.714 M	5.933 ± 0.093	5512.750 M	2.077 ± 0.057	5515.425 C	3.988 ± 0.176	5508.960 M	7.236 ± 0.111	5508.614 M	4.258 ± 0.055
5518.412 C	5.668 ± 0.092	5513.750 M	2.098 ± 0.057	5515.844 M	4.105 ± 0.092	5509.568 C	7.399 ± 0.265	5509.235 C	4.182 ± 0.069
5518.711 M	5.735 ± 0.090	5514.747 M	2.202 ± 0.060	5516.497 C	3.821 ± 0.169	5510.931 M	7.349 ± 0.113	5509.624 M	4.251 ± 0.055
5519.715 M	6.090 ± 0.096	5515.331 C	2.152 ± 0.070	5516.843 M	4.033 ± 0.090	5511.923 M	7.297 ± 0.112	5510.622 M	4.171 ± 0.054
5520.727 M	6.036 ± 0.095	5515.753 M	2.113 ± 0.058	5517.490 C	4.065 ± 0.180	5512.898 M	7.167 ± 0.110	5511.626 M	4.178 ± 0.054
5521.734 M	6.244 ± 0.098	5526.742 M	1.877 ± 0.051	5517.847 M	3.998 ± 0.089	5513.902 M	7.380 ± 0.114	5512.616 M	4.082 ± 0.053
5525.703 M	6.303 ± 0.099	5527.771 M	1.938 ± 0.053	5518.507 C	3.824 ± 0.169	5514.897 M	7.429 ± 0.114	5513.614 M	3.948 ± 0.051
5526.707 M	6.515 ± 0.102	5528.741 M	1.963 ± 0.054	5519.858 M	4.167 ± 0.093	5515.571 C	7.348 ± 0.264	5514.613 M	4.014 ± 0.052
5527.742 M	6.552 ± 0.103	5529.757 M	1.919 ± 0.053	5525.905 M	4.115 ± 0.092	5515.908 M	7.286 ± 0.112	5515.192 C	4.051 ± 0.066
5528.713 M	6.528 ± 0.102	5530.738 M	1.942 ± 0.053	5526.527 C	3.817 ± 0.169	5516.539 C	7.489 ± 0.269	5515.615 M	4.076 ± 0.053
5529.727 M	6.640 ± 0.104	5531.732 M	1.940 ± 0.053	5526.833 M	4.222 ± 0.094	5516.909 M	7.423 ± 0.114	5516.255 C	4.070 ± 0.067
5530.713 M	6.691 ± 0.105	5532.743 M	1.909 ± 0.052	5527.854 M	4.190 ± 0.094	5517.543 C	7.503 ± 0.269	5516.615 M	3.978 ± 0.051
5531.708 M	6.545 ± 0.103	5533.696 M	2.011 ± 0.055	5528.848 M	3.960 ± 0.089	5517.913 M	7.350 ± 0.113	5517.304 C	3.988 ± 0.065
5532.720 M	6.610 ± 0.104	5535.715 M	1.835 ± 0.050	5529.846 M	4.070 ± 0.091	5518.564 C	7.548 ± 0.271	5517.607 M	4.024 ± 0.066
5533.779 M	6.620 ± 0.104	5536.700 M	1.980 ± 0.054	5530.843 M	4.112 ± 0.092	5518.900 M	7.287 ± 0.112	5518.313 C	3.897 ± 0.050

Table 6
(Continued)

Mrk 335		Mrk1501		3C 120		Mrk 6		PG 2130+099	
HJD[a]	$F_{H\beta}$[b]	HJD[a]	$F_{H\beta}$[b]	HJD[a]	$F_{H\beta}$[b]	HJD[a]	$F_{H\beta}$[b]	HJD[a]	$F_{H\beta}$[b]
5536.782 M	6.387 ± 0.100	5537.646 M	1.925 ± 0.053	5531.843 M	3.869 ± 0.087	5519.919 M	7.366 ± 0.113	5519.611 M	3.925 ± 0.051
5537.343 C	6.411 ± 0.105	5538.327 C	1.885 ± 0.062	5532.836 M	3.777 ± 0.084	5523.907 M	7.241 ± 0.112	5525.241 C	4.150 ± 0.068
5537.760 M	6.377 ± 0.100	5538.680 M	1.892 ± 0.052	5533.850 M	3.813 ± 0.085	5526.592 C	7.480 ± 0.268	5525.599 M	3.962 ± 0.051
5538.767 M	6.205 ± 0.097	5539.312 C	1.979 ± 0.065	5535.825 M	3.823 ± 0.086	5526.896 M	7.428 ± 0.114	5526.603 M	3.941 ± 0.051
5539.284 C	6.565 ± 0.107	5539.675 M	1.866 ± 0.051	5536.843 M	3.730 ± 0.083	5527.918 M	7.304 ± 0.112	5527.627 M	4.054 ± 0.052
5539.762 M	6.389 ± 0.100	5540.692 M	1.931 ± 0.053	5537.838 M	3.790 ± 0.085	5528.910 M	7.038 ± 0.108	5528.606 M	3.989 ± 0.051
5540.763 M	6.286 ± 0.099	5541.674 M	1.983 ± 0.054	5538.838 M	3.809 ± 0.085	5529.915 M	7.305 ± 0.112	5529.614 M	4.130 ± 0.053
5541.764 M	6.195 ± 0.097	5542.665 M	1.872 ± 0.051	5539.366 C	4.074 ± 0.180	5530.902 M	7.175 ± 0.110	5530.607 M	4.056 ± 0.052
5542.755 M	6.372 ± 0.100	5543.670 M	1.791 ± 0.049	5539.832 M	3.812 ± 0.085	5531.907 M	7.358 ± 0.113	5531.602 M	4.076 ± 0.053
5543.759 M	6.136 ± 0.096	5546.644 M	1.954 ± 0.054	5540.842 M	3.789 ± 0.085	5532.898 M	7.431 ± 0.114	5532.615 M	4.032 ± 0.052
5544.724 M	6.266 ± 0.098	5549.701 M	1.950 ± 0.053	5541.830 M	3.769 ± 0.084	5533.913 M	7.248 ± 0.112	5533.613 M	4.066 ± 0.052
5545.732 M	6.177 ± 0.097	5550.705 M	1.893 ± 0.052	5542.869 M	3.751 ± 0.084	5535.888 M	7.469 ± 0.115	5536.610 M	4.010 ± 0.052
5546.734 M	6.292 ± 0.099	5556.634 M	1.873 ± 0.051	5543.827 M	3.748 ± 0.084	5536.910 M	7.534 ± 0.116	5538.168 C	3.924 ± 0.064
5549.606 M	6.203 ± 0.097	5559.655 M	1.873 ± 0.051	5544.805 M	3.692 ± 0.083	5537.909 M	7.829 ± 0.121	5538.607 M	3.864 ± 0.050
5550.671 M	6.252 ± 0.098	5568.214 C	1.989 ± 0.065	5545.822 M	3.693 ± 0.083	5538.478 C	7.488 ± 0.269	5539.225 C	4.025 ± 0.066
5555.713 M	6.306 ± 0.099			5546.841 M	3.898 ± 0.087	5538.898 M	8.056 ± 0.124	5539.607 M	3.904 ± 0.050
5556.720 M	6.434 ± 0.101			5549.793 M	3.695 ± 0.083	5539.467 C	7.455 ± 0.267	5540.602 M	3.976 ± 0.051
5557.716 M	6.512 ± 0.102			5557.796 M	3.698 ± 0.083	5539.894 M	7.989 ± 0.123	5541.573 M	3.870 ± 0.050
5559.711 M	6.497 ± 0.102			5559.789 M	3.543 ± 0.079	5540.904 M	7.887 ± 0.121	5542.595 M	4.000 ± 0.052
5568.247 C	6.578 ± 0.107			5569.322 C	3.397 ± 0.150	5541.896 M	7.859 ± 0.121	5543.598 M	3.848 ± 0.050
						5542.890 M	8.040 ± 0.124	5544.606 M	3.894 ± 0.050
						5543.894 M	8.074 ± 0.124	5548.607 M	3.879 ± 0.050
						5544.868 M	8.100 ± 0.125	5555.602 M	3.925 ± 0.051
						5545.890 M	7.959 ± 0.123	5557.596 M	3.891 ± 0.050
						5546.946 M	8.117 ± 0.125		
						5549.869 M	8.156 ± 0.126		
						5550.836 M	8.114 ± 0.125		
						5555.816 M	7.937 ± 0.122		
						5556.859 M	8.001 ± 0.123		
						5559.867 M	8.011 ± 0.123		

Notes. Observatory code: M = MDM Observatory and C = CrAO.
[a] Heliocentric Julian date (−2450000).
[b] Hβ flux is in units of 10^{-13} erg s^{-1}cm^{-2}.

Table 7
Light Curve Statistics

	Continuum Statistics					Hβ Statistics				
	Sampling (days)		Mean			Sampling (days)		Mean		
Objects	$\langle T \rangle$	T_{median}	Flux[a]	F_{var}	R_{max}	$\langle T \rangle$	T_{median}	Flux[a]	F_{var}	R_{max}
(1)	(2)	(3)	(4)	(5)	(6)	(7)	(8)	(9)	(10)	(11)
Mrk 335	1.1	0.96	7.49 ± 1.01	0.13	1.57 ± 0.04	1.5	1.00	5.74 ± 0.55	0.09	1.35 ± 0.03
Mrk 1501	0.66	0.48	1.49 ± 0.16	0.11	1.48 ± 0.04	1.55	0.99	2.16 ± 0.23	0.10	1.44 ± 0.05
3C 120	0.72	0.53	3.37 ± 0.38	0.11	1.49 ± 0.07	1.5	0.99	3.75 ± 0.24	0.06	1.28 ± 0.04
Mrk 6	0.84	0.58	8.93 ± 1.14	0.13	1.65 ± 0.04	1.2	0.99	7.00 ± 0.69	0.10	1.42 ± 0.04
PG 2130+099	0.55	0.43	3.1 ± 0.23	0.07	1.33 ± 0.03	1.32	0.99	4.17 ± 0.17	0.04	1.14 ± 0.02

Notes. Column 1 lists the object, Columns 2 and 3 list the average and median time spacing between continuum observations, respectively. Column 4 gives the mean flux of the continuum in the observed frame. Column 5 gives the excess variance, defined by

$$F_{var} = \frac{\sqrt{\sigma^2 - \delta^2}}{\langle f \rangle}, \quad (2)$$

where σ^2 is the flux variance of the observations, δ^2 is the mean square uncertainty, and $\langle f \rangle$ is the mean observed flux (Rodriguez-Pascual et al. 1997). Column 6 is the ratio of the maximum to minimum flux in each light curve. Columns 7–11 are the same quantities but computed using the merged Hβ light curves rather than the continuum light curves.
[a] Continuum and emission-line fluxes are given in 10^{-15} erg s^{-1} cm^{-2} Å^{-1} and 10^{-13} erg s^{-1} cm^{-2}, respectively, and have not been corrected for host galaxy contamination.

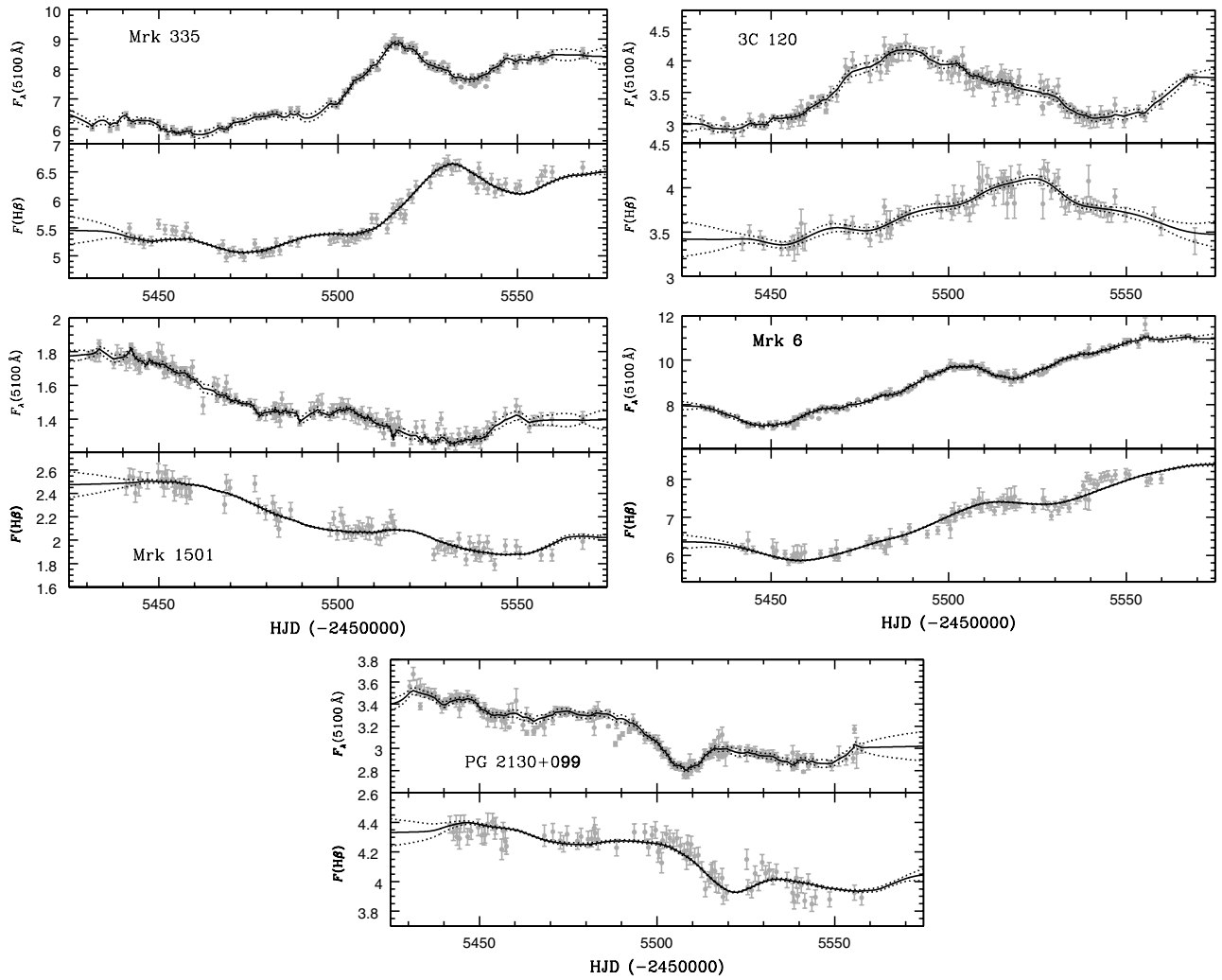

Figure 3. Mean of the predicted light curves and their dispersions as estimated by the best-fit SPEAR model. For each object, the top panel shows the continuum light curve, and the bottom panel shows the Hβ light curve, both in the same units as Figure 2. The gray points show the merged light curves used in the model, and the solid line shows the mean of the SPEAR light curve models fit to the data. Dotted black lines show the standard deviation of values about the mean (see Zu et al. 2011).

Table 8
Rest-frame Hβ Lag Measurements

Object	$\tau_{\rm SPEAR}$ (days)	$\tau_{\rm cent,CCF}$ (days)	$\tau_{\rm peak,CCF}$ (days)
(1)	(2)	(3	(4)
Mrk 335	$14.1^{+0.4}_{-0.4}$	14.3 ± 0.7	14.0 ± 0.9
Mrk 1501	$15.5^{+2.2}_{-1.8}$	12.6 ± 3.9	13.8 ± 5.4
3C 120	$27.2^{+1.1}_{-1.1}$	25.9 ± 2.3	25.6 ± 2.4
Mrk 6	$9.2^{+0.8}_{-0.8}$	10.1 ± 1.1	10.2 ± 1.2
PG 2130+099	$12.8^{+1.2}_{-0.9}$	9.6 ± 1.2	9.7 ± 1.3

be the case. However, the resulting CCFs were cleaner, with much more narrow and well-defined peaks when the trends were subtracted.

4.1. Line Width and $M_{\rm BH}$ Calculations

Assuming that the motion of the Hβ-emitting gas is dominated by gravity, the relation between $M_{\rm BH}$, line width, and time delay is

$$M_{\rm BH} = \frac{f c \tau \Delta V^2}{G}, \quad (1)$$

where τ is the measured emission-line time delay, ΔV is the velocity dispersion of the BLR, and f is a dimensionless factor that depends on the geometry, kinematics, and orientation of the BLR. The BLR velocity dispersion can be estimated using the observed Hβ line width. This line width can be characterized by either the FWHM or the line dispersion, $\sigma_{\rm line}$. To determine the best value of the line width and its uncertainty, we use Monte Carlo simulations similar to those used when determining the lag from the CCF. We run 100 simulations in which we create a mean and rms residual spectrum from a randomly chosen subset of the spectra, obtaining a distribution of resolution-corrected line widths. We take the mean value of $\sigma_{\rm line}$ or FWHM from these realizations and use their standard deviation as our uncertainty. We measure $\sigma_{\rm line}$ and FWHM in both the mean and rms residual spectra for completeness, and report these in Table 9. We use the rms residual spectrum line widths to estimate $M_{\rm BH}$, as this eliminates contamination from constant narrow-line components and isolates the broad-emission components that are actually responding to the continuum variations.

We adopt $\langle f \rangle = 5.5$. This estimate is based on the assumption that AGNs follow the same $M_{\rm BH}$–σ_* relationship as quiescent galaxies (Onken et al. 2004), and is consistent with Woo et al. (2010). This factor allows for easy comparison with previous results, but is about a factor of two larger than the value of $\langle f \rangle$ computed by Graham et al. (2011). We use $\sigma_{\rm line}$(rms) in our $M_{\rm BH}$ computation because there is at least some evidence

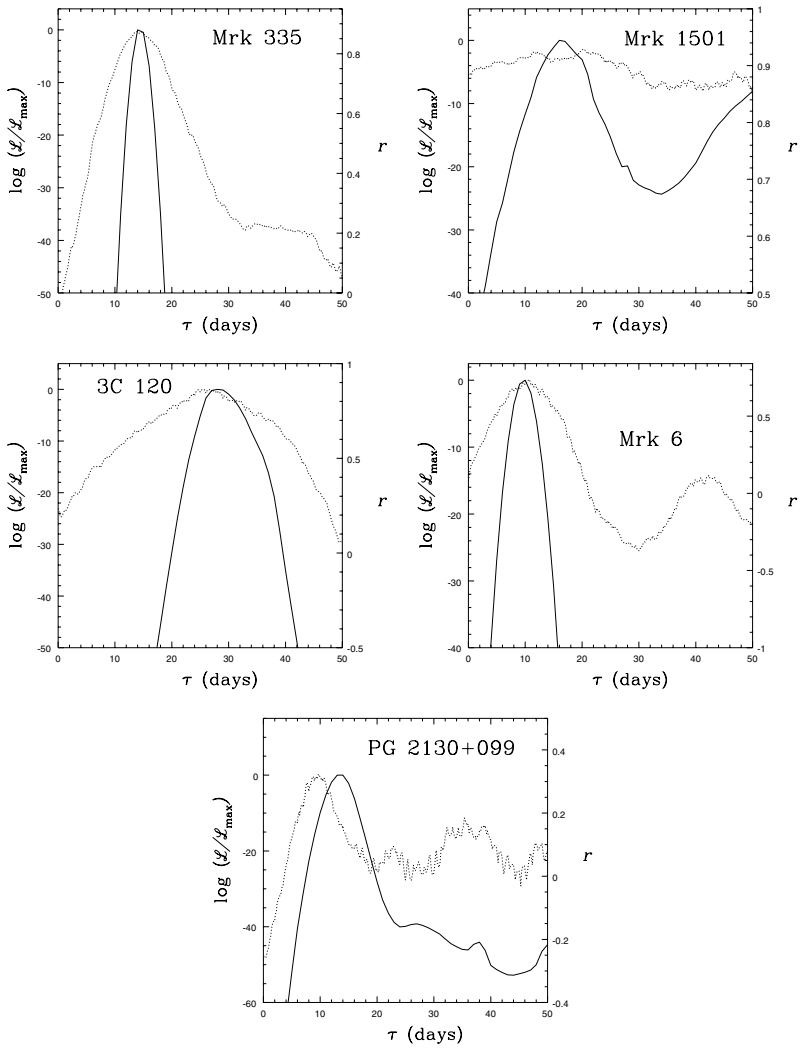

Figure 4. Lag estimates. The solid black lines show the log-likelihood functions from the SPEAR analyses, where the left axes show the SPEAR likelihood ratios log ($\mathscr{L}/\mathscr{L}_{\rm max}$). The dotted black lines show the cross-correlation functions, whose r values are shown on the right axes. The ranges of the y-axes were chosen for easy comparison between the two curves.

Table 9
Mean and RMS Line Widths, Virial Masses, and Luminosities

Object	$\sigma_{\rm line}$(mean) (km s^{-1})	FWHM(mean) (km s^{-1})	$\sigma_{\rm line}$(rms) (km s^{-1})	FWHM(rms) (km s^{-1})	$M_{\rm vir}$ ($\times 10^6\ M_\odot$)	$M_{\rm BH}$ ($\times 10^6\ M_\odot$)	log λL_{5100} (erg s^{-1})
(1)	(2)	(3)	(4)	(5)	(6)	(7)	(8)
Mrk 335	1663 ± 6	1273 ± 3	1293 ± 64	1025 ± 35	4.6 ± 0.5	25 ± 3	43.70 ± 0.08
Mrk 1501	3106 ± 15	3494 ± 35	3321 ± 107	5054 ± 145	33.4 ± 4.9	184 ± 27	44.32 ± 0.05
3C 120	1687 ± 4	1430 ± 16	1514 ± 65	2539 ± 466	12.2 ± 1.2	67 ± 6	43.96 ± 0.06
Mrk 6	4006 ± 6	2619 ± 24	3714 ± 68	9744 ± 370	24.8 ± 2.3	136 ± 12	43.75 ± 0.06
PG 2130+099	1760 ± 2	1781 ± 5	1825 ± 65	2097 ± 102	8.3 ± 0.7	46 ± 4	44.15 ± 0.03

that it produces less biased $M_{\rm BH}$ measurements than using the FWHM (Peterson 2011). Using $\tau_{\rm SPEAR}$ for the average time lag, we compute the virial product ($M_{\rm vir} = c\tau\Delta V^2/{\rm G}$) and $M_{\rm BH}$ for all five galaxies. The measurements are reported in Table 9.

5. DISCUSSION

5.1. The Radius–Luminosity Relationship

We compute the average 5100 Å luminosities of our sources, correcting for host-galaxy contamination following Bentz et al. (2009a). We measure the observed-frame host-galaxy flux in our aperture for each source using *Hubble Space Telescope* (*HST*) images (Table 3). With these measurements, we calculate the host-subtracted, rest-frame 5100 Å AGN luminosity for placement on the radius–luminosity relationship. The final host-subtracted AGN luminosities are given in Table 9. Note that we do not currently have *HST* images from which to measure the host luminosity for two of our objects, Mrk 6 and Mrk 1501. As a consequence, the luminosities listed for these objects are the total 5100 Å luminosities rather than just that of the AGN, and we expect them to fall to the right of the $R_{\rm BLR}$–L relationship.

Figure 5 shows the Bentz et al. (2009a) $R_{\rm BLR}$–L relationship and the placement of our new measurements. Previous measurements from Bentz et al. (2009a) are represented as open shapes,

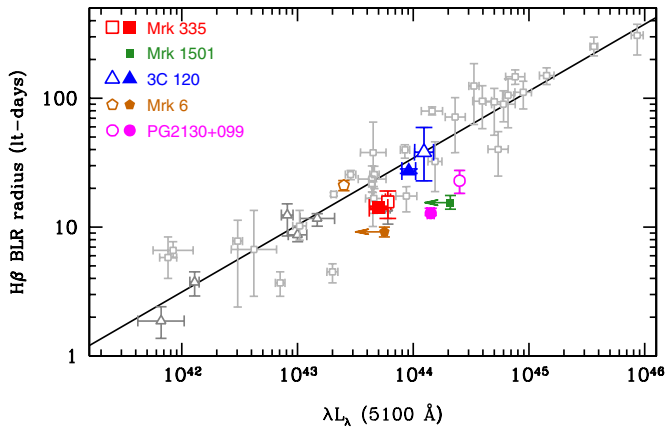

Figure 5. Relationship between the BLR radius and AGN luminosity at 5100 Å. The most recent calibration, from Bentz et al. (2009a), is shown by the solid line. Gray squares are from Bentz et al. (2009a) and darker gray triangles are from Denney et al. (2010). Open colored shapes show previous measurements for our sources from Bentz et al. (2009a). The orange open square representing Mrk 6 is from Doroshenko et al. (2012). Filled colored shapes represent our new measurements of these objects. Each source was given its own shape and color combination for ease of comparison between the new and old measurements. Note that Mrk 6 and Mrk 1501 do not have their host galaxy starlight subtracted and therefore their continuum luminosities are shown as upper limits.

(A color version of this figure is available in the online journal.)

while our new measurements are represented by filled shapes, varying in shape and color by object. We have not re-fit the best-fit trend including our new data; we leave this to a future work. Mrk 335 and 3C 120 both fall very close to their positions from the Bentz et al. (2009a), but we have increased the precision of their $R_{\rm BLR}$ measurements. PG2130 +099 continues to lie somewhat to the right of the relation. Both Mrk 6 and Mrk 1501 also lie noticeably below the relationship, as is expected since we were unable to subtract the host galaxy starlight—we therefore show these luminosity measurements as upper limits. Host measurements for these galaxies will shift both of them to lower luminosities and hence closer to the existing $R_{\rm BLR}$–L relation.

To see where we expect Mrk 1501 and Mrk 6 to lie on the relation after host subtraction, we examined the host galaxy light fraction in galaxies with similar BLR sizes (i.e., similar lags) to these two objects. Using measurements from Bentz et al. (2009a), we calculated the average fraction of host galaxy light among galaxies with similar lags, and used this fraction to calculate the expected host galaxy fluxes, and hence the expected host-subtracted luminosities, in Mrk 1501 and Mrk 6. Host galaxies in objects with lags similar to Mrk 1501 contributed on average 34% of the total luminosity, so we expect Mrk 1501 to change from $\log \lambda L_{5100} = 44.32 \pm 0.05$ to around 44.10. Host galaxies in objects with lags similar to Mrk 6 contributed on average 56% of the total luminosity. If we applied this to Mrk 6, the host-subtracted luminosity would then be $\log \lambda L_{5100} = 43.40$. Both of these objects will likely continue to lie below the current $R_{\rm BLR}$–L relation, but within the normal range of scatter currently observed. However, it is important to note that there is a very large scatter in the fraction of the luminosity contributed by the host galaxies in general, so these numbers are used for very rough estimations only.

5.2. Comments on Individual Objects

5.2.1. Mrk 335

Previous reverberation measurements of Mrk 335 were made by Kassebaum et al. (1997) and Peterson et al. (1998) and reanalyzed by Peterson et al. (2004) and Zu et al. (2011). Previous Hβ measurements for this object are quite good, and it was included in this study mainly for the potential to measure the size of the high-ionization component of the BLR. Details from our study have been reported by Grier et al. (2012), and the data have been included in this study for completeness. Our new measurement of $R_{\rm BLR} = 14.1^{+0.4}_{-0.4}$ days is consistent with the previous measurement of $R_{\rm BLR} = 15.3^{+3.6}_{-2.2}$ (Zu et al. 2011) when taking into account the luminosity change of Mrk 335 between these two campaigns. In other words, the position of Mrk 335 on the $R_{\rm BLR}$–L relationship changed predictably given the expected photoionization slope of $R \sim L^{1/2}$ (i.e., $\tau \sim L^{1/2}$).

5.2.2. Mrk 1501

No previous reverberation mapping measurements exist for Mrk 1501. We measure $\tau = 15.5^{+2.2}_{-1.9}$ days and a resulting black hole mass of $M_{\rm BH} = (1.84 \pm 0.27) \times 10^8\ M_\odot$. As noted above, this object lies noticeably to the right of the $R_{\rm BLR}$–L relation, which is expected since we have not yet subtracted the host galaxy contribution to the 5100 Å luminosity due to the lack of *HST* imaging data. As mentioned above, once we have corrected for host subtraction we expect the object to lie below the relation, but still within the normal scatter.

5.2.3. 3C 120

3C 120 was observed by Peterson et al. (1998) and reanalyzed by Peterson et al. (2004). The latter study reported $\tau_{\rm cent} = 39.4^{+22.1}_{-15.8}$ days, corresponding to $M_{\rm BH} = 5.55^{+3.14}_{-2.25} \times 10^7\ M_\odot$. We included 3C 120 in our campaign in an effort to reduce the large uncertainties in $R_{\rm BLR}$. Our new measurement of $\tau = 27.2^{+1.1}_{-1.1}$ days leads to $M_{\rm BH} = (6.7 \pm 0.6) \times 10^7\ M_\odot$, which is consistent with the previous measurements, but has much smaller uncertainties due to both better-sampled light curves and the improved techniques of measuring lags using SPEAR. Our new measurements place this object slightly below the $R_{\rm BLR}$–L relation, consistent with its previously measured position.

5.2.4. Mrk 6

Mrk 6 was observed in reverberation studies by Sergeev et al. (1999), Doroshenko & Sergeev (2003), and Doroshenko et al. (2012), who measured Hβ time lags using cross-correlation. Doroshenko et al. (2012) report $\tau_{\rm cent} = 21.1 \pm 1.9$ days. This measurement was used to calculate $M_{\rm BH} = (1.8 \pm 0.2) \times 10^8\ M_\odot$. This study used light curves that cover a very long time period with more sparse sampling than our campaign. Because of our dense time sampling, our light curves are sensitive to lags as small as a day or two. We measure an Hβ time lag of 9.2 ± 0.8 days and $M_{\rm BH} = (1.36 \pm 0.13) \times 10^8\ M_\odot$.

Our new τ measurement is substantially lower than the previous measurement—however, varying BLR sizes are expected if the luminosity of the object changes, in accordance with the $R_{\rm BLR}$–L relation. In this case, the previous study reports lower AGN luminosity measurements than we find, and by the $R_{\rm BLR}$–L relation we would also expect a smaller τ measurement in their data. However, they measure a lag on the order of twice the length of ours, so this difference cannot be explained by a change in the luminosity state. To investigate, we ran the light curves from Doroshenko et al. (2012) through both the CCF and SPEAR analysis software, and obtain results that are generally consistent with theirs to within errors when using cross-correlation. However, we do note that the lags we measure using SPEAR are noticeably lower than the lags they report when we

confine our attention to their more well-sampled light curves. For example, with their best-sampled light curves that cover the end of their observing period, we measure $\tau = 11.5^{+1.2}_{-0.8}$ days, where they report $\tau = 20.4^{4.6}_{-4.1}$ days for the same light curves. The median spacing between observations in the Doroshenko et al. (2012) light curves is always above 10 days, which we suspect renders their light curves insensitive to lags shorter than this. We are confident that our measurement of $\tau = 9.2$ days is accurate for our data set, as the lag signal is clearly visible in our light curves and the sampling rate is very high in both the continuum and Hβ light curves.

Mrk 6 has a very interesting Hβ profile (see Figure 1) that has been observed to change dramatically both in flux and shape (Doroshenko & Sergeev 2003, Sergeev et al. 1999). The rms line profile from our study is clearly double-peaked and shows significant blending of the He II emission with the Hβ emission. To verify that our line width measurement is not affected by the He II component, we fit a second-order polynomial to the He II feature in the rms spectrum and subtracted it from the total rms spectrum. We then re-measured the line width from this new spectrum and obtained a measurement consistent with that taken from the entire rms spectrum. This suggests that the He II blending did not affect our measurement of $\sigma_{\rm line}$, so we adopted our original measurement for use in the $M_{\rm BH}$ calculations. There are a variety of physical models that can produce this double-peaked profile, many of which we expect would show clear velocity-resolved signatures in our data. This analysis is beyond the scope of this paper and will be explored in detail in a future work.

5.2.5. PG 2130+099

Initial reverberation results for PG 2130+099 were first published by Kaspi et al. (2000), who measured a value of τ on the order of 200 days and thus inferred a BH mass of $1.4 \times 10^8\ M_\odot$. It was a significant outlier on both the $M_{\rm BH}$–σ_* and $R_{\rm BLR}$–L relations. However, PG 2130+099 was later re-observed and measured to have $R_{\rm BLR} = 22.9^{+4.4}_{-4.3}$ days and $M_{\rm BH} = (3.8 \pm 1.5) \times 10^7\ M_\odot$ (Grier et al. 2008), both of which are about an order of magnitude smaller than the original measurements. The discrepancy was attributed to undersampled light curves in the first measurements, as well as long-term secular changes in the Hβ equivalent width. While the 2008 data showed a clear reverberation signal, the amplitude of the variability in the study was quite low and the campaign was short in duration, rendering it insensitive to lags above 50 days, which made the light curves less than ideal. We included this object in our study in hopes of obtaining a better-sampled light curve sensitive to a wide range of time lags that would yield a more definitive result. Our new measurements of $\tau = 12.8^{+1.2}_{-0.9}$ days and $M_{\rm BH} = (4.6 \pm 0.4) \times 10^7\ M_\odot$ are consistent with those of Grier et al. (2008), but with higher precision. Note that PG 2130+099 is in a noticeably different position on the $R_{\rm BLR}$–L relation—it has moved nearly parallel to the relation from its previous location, since its luminosity has also changed. Like Mrk 335, this is consistent with the expectations from photoionization models of the BLR.

6. SUMMARY

We have presented reverberation measurements for five objects studied in our 2010 observational campaign. We successfully measured the average size of the Hβ-emitting region in all five objects. Four of these measurements constitute significant improvements in precision compared to previous measurements, and the fifth was the first reverberation measurement for the object. We also measured the line widths in these objects and used these to measure black hole masses, $M_{\rm BH}$, for the sample. In all cases, our new measurements are consistent with previous measurements, but with reduced uncertainties. We placed our objects on the most current $R_{\rm BLR}$–L relationship and find that our new measurements place our objects in locations consistent with previous measurements when taking into account the poorer precision of past measurements and observed mean luminosity changes. This is consistent with the location of the BLR being regulated by photoionization physics. We do not have host galaxy luminosity measurements for two of our objects, and these objects lie below the relation, as expected for objects with significant uncorrected host galaxy contamination in their luminosities (Bentz et al. 2009a).

Our work also demonstrates the utility of highly sampled light curves in reducing uncertainties in BLR radius measurements. A large sample of high-precision $R_{\rm BLR}$ and $M_{\rm BH}$ measurements, such as the measurements presented here, is crucial in understanding the intrinsic scatter in the $R_{\rm BLR}$–L relation as well as understanding the nature of other observed relations such as the $M_{\rm BH}$–σ_* and $M_{\rm BH}$–$L_{\rm Bulge}$ relationships. We will defer discussion of these relationships to a future contribution.

We gratefully acknowledge the support of the National Science Foundation through grant AST-1008882. B.J.S., C.B.H., and J.L.V. are supported by NSF Fellowships. C.S.K. and D.M.S. acknowledge the support of NSF grant AST-1004756. A.M.M. acknowledges the support of Generalitat Valenciana, grant APOSTD/2010/030. S.K. is supported at the Technion by the Kitzman Fellowship and by a grant from the Israel–Niedersachsen collaboration program. S.R. is supported at Technion by the Zeff Fellowship. S.G.S. acknowledges the support to CrAO in the frame of the "CosmoMicroPhysics" Target Scientific Research Complex Programme of the National Academy of Sciences of Ukraine (2007–2012). V.T.D. acknowledges the support of the Russian Foundation of Research (RFBR, project no. 09-02-01136a). The CrAO CCD cameras were purchased through the US Civilian Research and Development for Independent States of the Former Soviet Union (CRDF) awards UP1-2116 and UP1-2549-CR-03. This research has been partly supported by the Grant-in-Aids of Scientific Research (17104002, 20041003, 21018003, 21018005, 22253002, and 22540247) of the Ministry of Education, Science, Culture and Sports of Japan. This research has made use of the NASA/IPAC Extragalactic Database (NED) which is operated by the Jet Propulsion Laboratory, California Institute of Technology, under contract with the National Aeronautics and Space Administration.

REFERENCES

Alard, C. 2000, A&AS, 144, 363
Alard, C., & Lupton, R. H. 1998, ApJ, 503, 325
Bentz, M. C., Peterson, B. M., Netzer, H., Pogge, R. W., & Vestergaard, M. 2009a, ApJ, 697, 160
Bentz, M. C., Peterson, B. M., Pogge, R. W., & Vestergaard, M. 2009b, ApJ, 694, L166
Bentz, M. C., Walsh, J. L., Barth, A. J., et al. 2009c, ApJ, 705, 199
Bertin, E., & Arnouts, S. 1996, A&AS, 117, 393
Blandford, R. D., & McKee, C. F. 1982, ApJ, 255, 419
Dasyra, K. M., Tacconi, L. J., Davies, R. I., et al. 2007, ApJ, 657, 102
Davidson, K. 1972, ApJ, 171, 213
Davidson, K., & Netzer, H. 1979, Rev. Mod. Phys., 51, 715
Denney, K. D., Peterson, B. M., Pogge, R. W., et al. 2010, ApJ, 721, 715

Di Matteo, T., Springel, V., & Hernquist, L. 2005, Nature, 433, 604
Doroshenko, V. T., & Sergeev, S. G. 2003, A&A, 405, 909
Doroshenko, V. T., Sergeev, S. G., Klimanov, S. A., Pronik, V. I., & Efimov, Y. S. 2012, arXiv:1203.2084
Ferrarese, L., & Merritt, D. 2000, ApJ, 539, L9
Gaskell, C. M., & Peterson, B. M. 1987, ApJS, 65, 1
Gaskell, C. M., & Sparke, L. S. 1986, ApJ, 305, 175
Gebhardt, K., Bender, R., Bower, G., et al. 2000, ApJ, 539, L13
Graham, A. W., Onken, C. A., Athanassoula, E., & Combes, F. 2011, MNRAS, 412, 2211
Greene, J. E., & Ho, L. C. 2007, ApJ, 667, 131
Greene, J. E., Peng, C. Y., Kim, M., et al. 2010, ApJ, 721, 26
Grier, C. J., Peterson, B. M., Bentz, M. C., et al. 2008, ApJ, 688, 837
Grier, C. J., Peterson, B. M., Pogge, R. W., et al. 2012, ApJ, 744, L4
Gültekin, K., Richstone, D. O., Gebhardt, K., et al. 2009, ApJ, 698, 198
Hopkins, P. F., Murray, N., & Thompson, T. A. 2009, MNRAS, 398, 303
Jahnke, K., & Macciò, A. V. 2011, ApJ, 734, 92
Kaspi, S., Smith, P. S., Netzer, H., et al. 2000, ApJ, 533, 631
Kassebaum, T. M., Peterson, B. M., Wanders, I., et al. 1997, ApJ, 475, 106
Kelly, B. C., Bechtold, J., & Siemiginowska, A. 2009, ApJ, 698, 895
Kelly, B. C., Vestergaard, M., Fan, X., et al. 2010, ApJ, 719, 1315
Kollmeier, J. A., Onken, C. A., Kochanek, C. S., et al. 2006, ApJ, 648, 128
Kormendy, J., & Richstone, D. 1995, ARA&A, 33, 581
Kozłowski, S., Kochanek, C. S., Udalski, A., et al. 2010, ApJ, 708, 927
MacLeod, C. L., Ivezić, Ž., Kochanek, C. S., et al. 2010, ApJ, 721, 1014
Magorrian, J., Tremaine, S., Richstone, D., et al. 1998, AJ, 115, 2285
Marziani, P., & Sulentic, J. W. 2012, New Astron. Rev., 56, 49
Mathur, S., Fields, D., Peterson, B. M., & Grupe, D. 2011, ApJ, submitted
Morgan, C. W., Kochanek, C. S., Morgan, N. D., & Falco, E. E. 2010, ApJ, 712, 1129
Onken, C. A., Ferrarese, L., Merritt, D., et al. 2004, ApJ, 615, 645
Peng, C. Y. 2007, ApJ, 671, 1098
Peng, C. Y. 2010, arXiv:1002.2664
Perez, E., Robinson, A., & de La Fuente, L. 1992, MNRAS, 255, 502
Peterson, B. M. 1993, PASP, 105, 247
Peterson, B. M. 2011, in Narrow-Line Seyfert 1 Galaxies and Their Place in the Universe, Proceedings of Science, POS(NLS1)032 http://pos.sissa.it/cgi-bin/reader/conf.cgi?confid=126
Peterson, B. M., Pogge, R. W., Wanders, I., Smith, S. M., & Romanishin, W. 1995, PASP, 107, 579
Peterson, B. M., Wanders, I., Bertram, R., et al. 1998, ApJ, 501, 82
Peterson, B. M., Ferrarese, L., Gilbert, K. M., et al. 2004, ApJ, 613, 682
Rodriguez-Pascual, P. M., Alloin, D., Clavel, J., et al. 1997, ApJS, 110, 9
Schlegel, D. J., Finkbeiner, D. P., & Davis, M. 1998, ApJ, 500, 525
Sergeev, S. G., Doroshenko, V. T., Golubinskiy, Y. V., Merkulova, N. I., & Sergeeva, E. A. 2005, ApJ, 622, 129
Sergeev, S. G., Pronik, V. I., Sergeeva, E. A., & Malkov, Y. F. 1999, ApJS, 121, 159
Shappee, B. J., & Stanek, K. Z. 2011, ApJ, 733, 124
Shen, Y., Greene, J. E., Strauss, M. A., Richards, G. T., & Schneider, D. P. 2008, ApJ, 680, 169
Silk, J., & Rees, M. J. 1998, A&A, 331, L1
Thévenaz, P., Blu, T., & Unser, M. 2000, IEEE Trans. Med. Imag., 19, 739
Tremaine, S., Gebhardt, K., Bender, R., et al. 2002, ApJ, 574, 740
van Groningen, E., & Wanders, I. 1992, PASP, 104, 700
Vestergaard, M., Fan, X., Tremonti, C. A., Osmer, P. S., & Richards, G. T. 2008, ApJ, 674, L1
Vestergaard, M., & Osmer, P. S. 2009, ApJ, 699, 800
Welsh, W. F. 1999, PASP, 111, 1347
White, R. J., & Peterson, B. M. 1994, PASP, 106, 879
Whittle, M. 1992, ApJS, 79, 49
Woo, J.-H., Treu, T., Barth, A. J., et al. 2010, ApJ, 716, 269
Zu, Y., Kochanek, C. S., Kozłowski, S., & Udalski, A. 2012, arXiv:1202.3783
Zu, Y., Kochanek, C. S., & Peterson, B. M. 2011, ApJ, 735, 80